The ubiquitin ligase Mindbomb 1 coordinates gastrointestinal secretory cell maturation

Benjamin J. Capoccia,[1] Ramon U. Jin,[1] Young-Yun Kong,[2] Richard M. Peek Jr.,[3] Matteo Fassan,[4] Massimo Rugge,[4] and Jason C. Mills[1]

[1]Division of Gastroenterology, Departments of Medicine, Developmental Biology, and Pathology and Immunology, Washington University School of Medicine, St. Louis, Missouri, USA. [2]Department of Biological Sciences, Seoul National University, Seoul, Republic of Korea. [3]Division of Gastroenterology, Hepatology, and Nutrition, Vanderbilt University School of Medicine, Nashville, Tennessee, USA. [4]Pathology and Cytopathology Unit, Department of Medicine, University of Padua, Padua, Italy.

After cell fate specification, differentiating cells must amplify the specific subcellular features required for their specialized function. How cells regulate such subcellular scaling is a fundamental unanswered question. Here, we show that the E3 ubiquitin ligase Mindbomb 1 (MIB1) is required for the apical secretory apparatus established by gastric zymogenic cells as they differentiate from their progenitors. When *Mib1* was deleted, death-associated protein kinase–1 (DAPK1) was rerouted to the cell base, microtubule-associated protein 1B (MAP1B) was dephosphorylated, and the apical vesicles that normally support mature secretory granules were dispersed. Consequently, secretory granules did not mature. The transcription factor MIST1 bound the first intron of *Mib1* and regulated its expression. We further showed that loss of MIB1 and dismantling of the apical secretory apparatus was the earliest quantifiable aberration in zymogenic cells undergoing transition to a precancerous metaplastic state in mouse and human stomach. Our results reveal a mechanistic pathway by which cells can scale up a specific, specialized subcellular compartment to alter function during differentiation and scale it down during disease.

Introduction

Once a cell commits to a specific cell fate and differentiates, it must be able to amplify the specific subcellular machinery it needs to perform its specialized cell function. Such specification requires scaling up the expression of genes that promote those processes. Recent work has identified a handful of transcription factors whose expression programs and drives the upregulation of defined subcellular processes, regardless of cell type. We have termed such transcriptional regulators *scaling factors* (1). For example, x-box binding protein 1 (XBP1) is necessary and sufficient to induce ER formation in diverse cells such as antigen-secreting plasma cells (2, 3) and gastric zymogenic cells (ZCs) (4), and the BHLH-ZIP transcription factor TFEB upregulates lysosome formation in diverse cell types (5, 6). In the absence of these factors, cells still adopt the correct fates and make ER and lysosomes, but they are unable to amplify the subcellular components that are key to their specialized mature functions. How such transcriptional regulators can induce changes in specific subcellular compartments simply by modulating expression levels of specific gene cohorts is a complex problem that is fundamental to understanding how cells develop and maintain their specialized physiological functions, particularly how these cellular decisions and functions are organized in a tissue under homeostatic conditions and perturbed during pathologic conditions.

The adult mammalian gastric epithelium undergoes constant renewal throughout life, providing a useful system for studying the role of scaling factors and developmentally regulated genes during cell maturation in the adult. For example, as mucus-secreting neck cells in the middle portion of the gastric unit (i.e., the neck) mature, they migrate toward the unit's base, at which point they undergo a series of substantial morphological changes that culminate in the formation of postmitotic, digestive enzyme–secreting ZCs (Figure 1A). The molecular processes underlying this elaborate transition are of particular relevance, as alterations in neck cell–ZC differentiation occur during gastric atrophy and metaplasia, processes that predispose to cancer (7–11). Stomach cancer is the fourth most common and second most fatal malignancy worldwide; however, the molecular and morphological progressions that cause this malignancy are unclear (12–14).The transcription factor MIST1 (encoded by *Mist1*; also known as *Bhlha15*) is critical for regulating normal neck cell–to–ZC maturation, and its expression is lost in gastric epithelial atrophy and metaplasia in both humans and mice (7, 15, 16). Thus, MIST1 may play a protective role.

Loss of MIST1 affects ZC maturation (16). During maturation of ZCs, which are exocrine secretory cells, the subcellular region between their nuclei and the apical lumen, into which the secretion of digestive enzymes is directed, is greatly expanded. This apical expansion is likely critical for maintenance of the stores of secretory granules that must be released upon agonist stimulation; however, neither the functional significance nor the molecular underpinnings of this maturational scaling process have been elucidated. Here, we present evidence that MIST1 directs the maturation of secretory granules and the apical expansion in ZCs by activating the expression of Mindbomb 1 (MIB1), a multidomained RING-finger type E3 ubiquitin ligase that is conserved from *Drosophila* to mammals (17–20). MIB1 is abundantly expressed throughout development and in adult tissues (21). In mammals, MIB1 was originally described as the key factor mediating the subcellular localization and turnover of death-associated protein kinase–1 (DAPK1) (21, 22). In addition, during embryonic development, MIB1 ubiquitinates the Notch ligands Delta and Jagged, rendering them competent to signal to and activate Notch in adjacent cells (19, 23–27). Thus, the role of MIB1 in cells in culture and

Conflict of interest: The authors have declared that no conflict of interest exists.
Citation for this article: *J Clin Invest.* 2013;123(4):1475–1491. doi:10.1172/JCI65703.

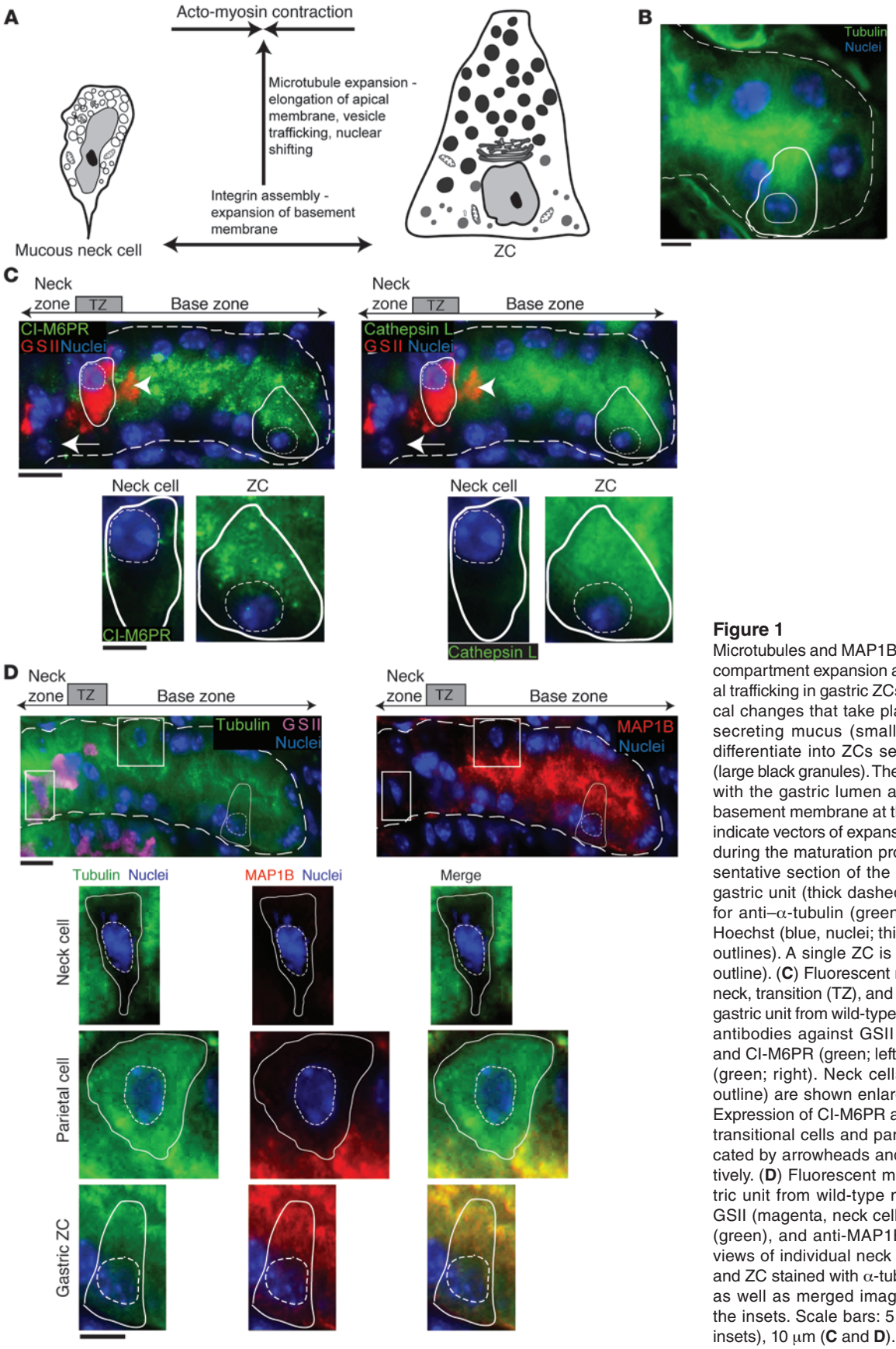

Figure 1
Microtubules and MAP1B coordinate apical compartment expansion and endolysosomal trafficking in gastric ZCs. (**A**) Morphological changes that take place as neck cells secreting mucus (small white granules) differentiate into ZCs secreting zymogen (large black granules). The cells are oriented with the gastric lumen at the top and the basement membrane at the bottom. Arrows indicate vectors of expansion or contraction during the maturation process. (**B**) Representative section of the base zone of the gastric unit (thick dashed outline) stained for anti–α-tubulin (green) antibodies and Hoechst (blue, nuclei; thin dashed or solid outlines). A single ZC is highlighted (solid outline). (**C**) Fluorescent microscopy of the neck, transition (TZ), and base zones of the gastric unit from wild-type mice stained with antibodies against GSII (red, neck cells) and CI-M6PR (green; left) and cathepsin L (green; right). Neck cells and ZCs (solid outline) are shown enlarged in the insets. Expression of CI-M6PR and cathepsin L in transitional cells and parietal cells is indicated by arrowheads and arrows, respectively. (**D**) Fluorescent microscopy of gastric unit from wild-type mice stained with GSII (magenta, neck cells), anti–α-tubulin (green), and anti-MAP1B (red). Enlarged views of individual neck cell, parietal cell, and ZC stained with α-tubulin and MAP1B, as well as merged images, are shown in the insets. Scale bars: 5 μm (**B**; **C** and **D**, insets), 10 μm (**C** and **D**).

Table 1
ZC-specific genes categorized under the GO term "microtubule"

Probe set	Gene symbol	Gene name	Accession	Fold change
10432404	*Tuba1a*	Tubulin, alpha 1A	NM_011653	2.98
10447224	*Dync2li1*	Dynein cytoplasmic 2 light intermediate chain 1	NM_172256	2.93
10520544	*Mapre3*	Microtubule-associated protein, RP/EB family, member 3	NM_133350	2.9
10518585	*Kif1b*	Kinesin family member 1B	NM_207682	2.48
10360479	*Cep170*	Centrosomal protein 170	NM_001099637	2.1
10387180	*Ndel1*	Nuclear distribution gene E-like homolog 1 (*A. nidulans*)	NM_023668	1.92
10408610	*Tubb2a*	Tubulin, beta 2a	NM_009450	1.91
10359480	*Dnm3*	Dynamin 3	NM_001038619	1.8
10560491	*Klc3*	Kinesin light chain 3	NM_146182	1.76
10420320	*Cenpj*	Centromere protein J	NM_001014996	1.7
10411519	*Mtap1b*	Microtubule-associated protein 1B	NM_008634	1.67
10408975	*Kif13a*	Kinesin family member 13A	NM_010617	1.62
10572516	*Mtap1s*	Microtubule-associated protein 1S	NM_173013	1.55
10587368	*Mto1*	Mitochondrial translation optimization 1 homolog (*S. cerevisiae*)	NM_026658	1.53
10533659	*Clip1*	CAP-GLY domain containing linker protein 1	NM_019765	1.5
10475293	*Tubgcp4*	Tubulin, gamma complex associated protein 4	NM_153387	1.49
10589541	*Kif9*	Kinesin family member 9	NM_010628	1.45
10398727	*Klc1*	Kinesin light chain 1	NM_001025360	1.45
10433721	*Nde1*	Nuclear distribution gene E homolog 1 (*A. nidulans*)	NM_023317	1.45
10557233	*Tnrc6a*	Trinucleotide repeat containing 6a	NM_144925	1.45
10576056	*Map1lc3b*	Microtubule-associated protein 1 light chain 3 beta	NM_026160	1.44
10477353	*Mapre1*	Microtubule-associated protein, RP/EB family, member 1	NM_007896	1.44
10454655	*Apc*	Adenomatosis polyposis coli	NM_007462	1.41
10603567	*Dynlt3*	Dynein light chain Tctex-type 3	NM_025975	1.41

in early embryonic development is well delineated, but how MIB1 governs the homeostasis or maturation of terminally differentiated cells in the adult organism remains unclear.

Here, we took advantage of the spatiotemporally ordered development of the gastric ZC lineage to study the cellular and molecular mechanisms underlying the expansion and maturation of the apical cytoplasmic compartment. We found that deletion of MIB1 specifically in adult mature ZCs caused abnormal subcellular localization of DAPK1, loss of phosphorylated apical MAP1B (encoded by *Mtap1b*), apical reorientation of nuclei, and defective late endosome trafficking. We showed that MIST1 bound to the 5′ regulatory region of *Mib1*, and loss of MIST1 caused loss of ZC-specific MIB1 expression, mislocalization of DAPK1 in ZCs, and abrogation of the MIB1-DAPK1 protein interaction. Relevant to cancer progression, we showed using mouse models and human specimens that loss of MIB1 expression, and dismantling of the apical digestive enzyme secretory apparatus, was the earliest detectable aberration in ZCs undergoing spasmolytic polypeptide–expressing metaplasia (SPEM). Indeed, scaling down of the MIB1-regulated apical secretory apparatus predated upregulation of mucous neck cell proteins like spasmolytic polypeptide (also known as TFF2), which is how this lesion was named and has been traditionally diagnosed. The present study is the first to describe a molecular mechanism that regulates a prosecretory apical compartment in physiologically mature cells, as well as a function for MIB1 both in the normal stomach and en route to cancer.

Results

The apical compartment specifically expands during ZC maturation. As mucous neck cells migrate into the base segment of the gastric unit, they undergo a series of well-characterized, highly coordinated morphological changes that culminate in the formation of postmitotic, digestive enzyme–producing ZCs (7, 16, 28). Vectors associated with changes in architecture during ZC maturation are shown in Figure 1A. During maturation, the luminal apex of the ZC shows concentration of subcortical F-actin and nonmuscle myosin II, while the basal membrane expands with the establishment of integrin–extracellular matrix connections (Supplemental Figure 1; supplemental material available online with this article; doi:10.1172/JCI65703DS1). Concomitant with these processes, the apical compartment of the cell expands greatly, as the cells enlarge with digestive enzyme–secretory vesicles and the nucleus migrates to the base.

In the current study, we focused on the cellular and molecular mechanisms that lead to the dramatic expansion of the apical region of the cell. Our hypothesis was that maturation and expansion of the apical cellular compartment is a fundamental cell process that facilitates the large-capacity polarized storage and regulated secretion of digestive enzymes key to the physiology of these cells. To understand how changes in the apical cytoplasmic compartment are coordinated at the genetic level, we performed gene expression profiling: RNA from purified populations of neck cells and ZCs was isolated using multilabel, RNA-preserving laser capture microdissection (LCM) (16), linearly amplified, and hybridized to Affymetrix Mouse Gene 1.0ST arrays. Genes whose expression was enriched in ZCs compared with neck cells were identified, and 2,935 such ZC-specific genes were generated and sorted based on Gene Ontology (GO) using GOurmet software (29, 30). The fractional representation of genes categorized by the GO term "microtubule" was overrepresented in ZCs (Table 1). Gene expression of α-tubulin in ZCs increased 3-fold compared with neck cells (*Tuba1a*; Table 1),

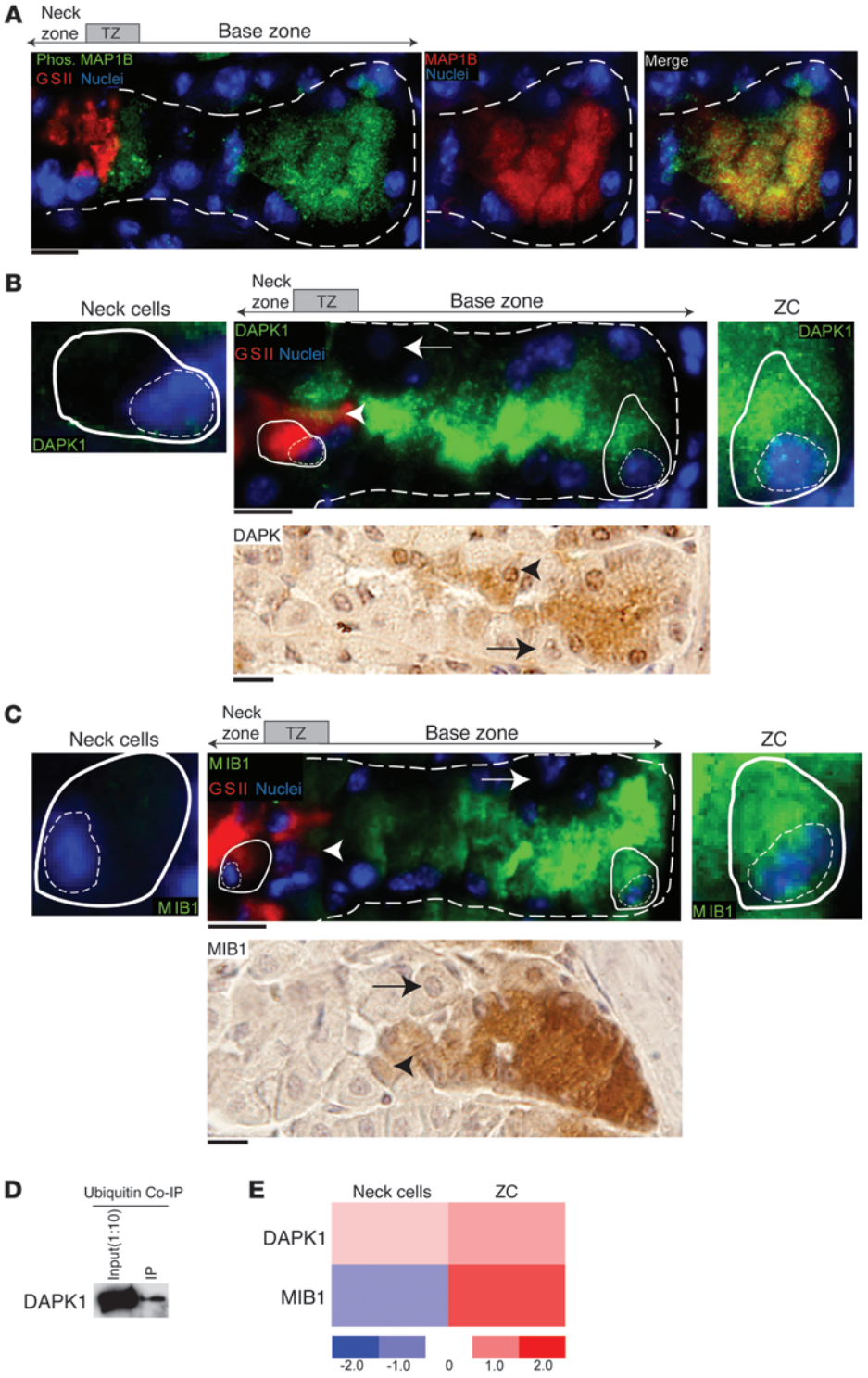

Figure 2
The DAPK1-MIB1 protein complex is localized to the apical compartment of ZCs. (**A**) Fluorescent microscopy of an individual gastric unit (thick dashed outline) stained with GSII (red) and an antibody that specifically recognizes MAP1B phosphorylated at Thr1265 (green). Insets show pan-MAP1B expression (red) and the merged image of the base zone of the gastric unit (far right). (**B** and **C**) Gastric units were stained with GSII (red), DAPK1 (**B**; green) or MIB1 (**C**; green), and Hoechst (blue, nuclei; thin dashed outline). Enlarged views (×1.5-fold) of representative neck cell and ZC (solid outline) are shown in insets. DAPK1 (**B**) or MIB1 (**C**) immunohistochemical staining (brown) is shown below. DAPK1 and MIB1 expression in the transition zone is indicated by arrowheads; lack of DAPK1 or MIB1 expression in parietal cells is indicated by arrows. (**D**) Western blot of ubiquitin immunoprecipitates for DAPK1. (**E**) Heatmap representing expression values of DAPK1 and MIB1 probesets in neck cells and ZCs. Scale bars: 10 μm.

which would be expected to lead to dramatic expansion of tubulin mass, given the abundance of this ubiquitous cytoskeletal protein. Using immunofluorescence (IF) and confocal analyses, we confirmed the dramatic increase in the apical microtubular network relative to neck cells and how the elaborate microtubular expansion coordinated with movement of ZC nuclei toward the cell base (Figure 1, B and D).

Microtubules regulate cell shape and polarity and are the principal conduit for cellular vesicular trafficking (31–36); thus, we reasoned that the expansion of microtubules might also help coordinate expansion of apical vesicular trafficking. Mature lysosomes, identified by expression of LAMP1, LAMP2, and cathepsin D, localized to the subnuclear basal compartment (R.U. Jin and J.C. Mills, unpublished observations), and early (i.e., EEA1-positive)

endosomes showed no specific subcellular distribution (data not shown). We found a LAMP1-negative vesicular compartment, defined by expression of the cation-independent mannose-6-phosphate receptor (CI-M6PR) and by dramatic expansion of the proprotein convertase cathepsin L in the cell apex (Figure 1C). In cells with secretory granule stores, LAMP1-negative, and cathepsin L– and CI-M6PR–positive vesicles define a specific late endosomal and/or multivesicular body compartment involved in secretory granule maturation (37–41). This vesicular compartment was not detectable with these markers in neck cells (Figure 1C, insets) and parietal cells (Figure 1C, white arrows).

The stability and polarity of the microtubule network in ZCs are regulated by microtubule-associated proteins (MAPs) (32, 42). Additionally, microtubules in conjunction with MAPs facilitate spatial arrangements among the vesicular components of the secretory and endolysosomal pathways (33–35). We examined expression of 2 of the MAPS most increased during ZC maturation, *Mtap1b* and *Mtap1s* (Table 1). MAP1B and MAP1S protein expression was specific for ZCs compared with neck cells and also was localized specifically to the apical compartment (Figure 1D and data not shown; results for MAP1B and for MAP1S were equivalent). Collectively, these data showed that the dramatic expansion of the apical ZC compartment during maturation was correlated with elaboration of a microtubular network, specific trafficking of late endosomal vesicles and/or multivesicular bodies, and an increase in a microtubule coordinating protein, MAP1B, that is known to play a role in establishing polarized cell growth (43–45).

Apical localization of DAPK1 and apical expansion as a whole require MIB1. MAP regulation of microtubule dynamics in health and disease depends on regulated phosphorylation and dephosphorylation cycles (43, 44, 46). Using an antibody specific for MAP1B phosphorylated at Thr1265, an important functional phosphorylation site (43), we showed that much of the apical MAP1B in ZCs was phosphorylated (Figure 2A). Previous studies have shown that MAPs such as MAP1B are substrates for several serine/threonine kinases, including DAPK1 (43, 46–48).

The ability of DAPK1 to phosphorylate its downstream effectors is strongly influenced by its location in the cytoplasm, which in turn is mediated by its direct interaction with the E3 ubiquitin ligase MIB1 (21, 22, 49). Both DAPK1 and MIB1 protein expression increased as ZCs began to leave the neck/base transition zone (Figure 2, B and C, arrowheads), and both localized apically, as confirmed by confocal microscopy. Neither DAPK1 nor MIB1 protein was detectable in parietal cells (Figure 2, B and C, arrows). Consistent with previous data demonstrating MIB1-dependent ubiquitination of DAPK1 (21, 22), IP of stomachs with anti-ubiquitin antibodies demonstrated that a pool of DAPK1 was indeed ubiquitinated (Figure 2D). *DAPK1* gene expression was maintained at significant levels in both neck cells and ZCs, but was unchanged between the 2 cell populations (mean Affymetrix expression values, neck cells, 66 ± 5; ZCs, 72 ± 4; Figure 2E), consistent with its known posttranscriptional regulation by MIB1 (21). In contrast, expression of *MIB1* was substantially increased in ZCs versus neck cells (158 ± 5 vs. 53 ± 5; Figure 2E).

MIB1 regulates cell morphology, membrane trafficking (specifically late endosomal vesicles), and protein sorting (19, 50–52), although MIB1 function in the adult stomach has not been reported. We hypothesized that the dramatic apical expansion of ZCs as they mature from neck cells could be governed at the molecular level by induction of *MIB1* gene expression, which would cause apical localization and stabilization of DAPK1, in turn helping to coordinate apical vesicular trafficking and cytoskeletal expansion via MAP1B. We therefore bred floxed *Mib1* (*Mib1*$^{\Delta/\Delta}$) mice (24) with *Mist1*^{CreER} mice (53) to conditionally delete *Mib1* in mature, MIST1-expressing ZCs. Induction of Cre recombinase caused loss of MIB1 in nearly all basal ZCs by 2 weeks (Figure 3A). Subsequently, new wild-type ZCs, arising from mucous cell precursors migrating from the neck zone, slowly replaced *Mib1*$^{\Delta/\Delta}$ ZCs until none remained by 6 weeks (Figure 3 and data not shown). We used the 2-week time point for all subsequent experiments.

Consistent with our hypothesis that MIB1 regulates DAPK1 localization in the apical cytoplasm of ZCs, *Mib1*$^{\Delta/\Delta}$ ZCs showed striking relocalization of DAPK1 from the supranuclear to the subnuclear region of the cytoplasm (Figure 3B). As hypothesized, loss of apical localization caused loss of DAPK1 activity, as its substrate MAP1B was no longer detectable there in its phosphorylated form (Figure 3C). Loss of MIB1, apical DAPK1, and phosphorylated MAP1B all correlated with decreased apical trafficking of the CI-M6PR/cathepsin L compartment that normally expanded during neck cell–to–ZC maturation (Figure 3, D and E). Furthermore, the activated form of cathepsin L was increased in *Mib1*$^{\Delta/\Delta}$ ZCs, indicative of loss of the pro–cathepsin L form that normally traffics to the late endosomal compartment (37, 40). Finally, we observed that loss of MIB1 led to a dramatic accumulation of galectin 8, a marker of damaged endolysosomes (54), in the apex of *Mib1*$^{\Delta/\Delta}$ ZCs versus controls, whereas it was normally confined to the ZC bases, where autophagic/lysosomal activity was most prominent (Figure 3F). These results were confirmed by confocal microscopy (data not shown). Overall, our findings indicated that MIB1 is required for the apical expansion of the cytoskeleton and normal vesicular trafficking that characterize ZC maturation.

Mib1$^{\Delta/\Delta}$ ZCs did not reexpress mucous neck cells markers such as GSII (Figure 3 and Supplemental Figure 2) or reenter the cell cycle (Supplemental Figure 2A), as occurs when ZCs become metaplastic (55). In addition, loss of MIB1 in ZCs did not affect cleavage of the Notch1 receptor in the mature gastric epithelium, which remained in the isthmal region (Supplemental Figure 2B), where Notch has been described to play a role in regulating proliferation of the stem/progenitor cell (56). Loss of MIB1 also did not affect the protein expression level of Notch signaling intermediates Hes1 and Hes5 in ZCs or in any other gastric cells, as determined by histology (data not shown). Hence, the effects of MIB1 loss were not likely the result of non–ZC-autonomous effects due to aberrant Notch signaling.

MIB1 is expressed in a MIST1-dependent fashion during ZC differentiation. We next investigated the molecular regulation of *Mib1* gene expression. Previous studies have determined a critical role for MIST1 in regulating neck cell–to–ZC maturation (4, 7, 15, 16, 57). To determine whether *Mib1* expression is dependent upon MIST1 in the ZC lineage, gene expression profiles of neck cells and ZCs from *Mist1*$^{-/-}$ mice were prepared by LCM as described above. Whereas *Mib1* and *Mist1* transcripts were enriched concomitantly in ZCs compared with neck cells in age-matched wild-type mice, *Mib1* expression did not increase in *Mist1*$^{-/-}$ ZCs beyond the levels observed in neck cells (Figure 4A). These results were confirmed by PCR (data not shown). Similarly, MIB1 protein was detected only in transition cells just beginning to migrate out of the neck and into the base (Figure 4B, arrow), whereas mature *Mist1*$^{-/-}$ ZCs showed no detectable MIB1, and overall MIB1 protein levels were greatly reduced in *Mist1*$^{-/-}$ stomachs. Thus, loss of MIST1 reduced *Mib1* expression, which suggests that MIB1 is a downstream target of MIST1.

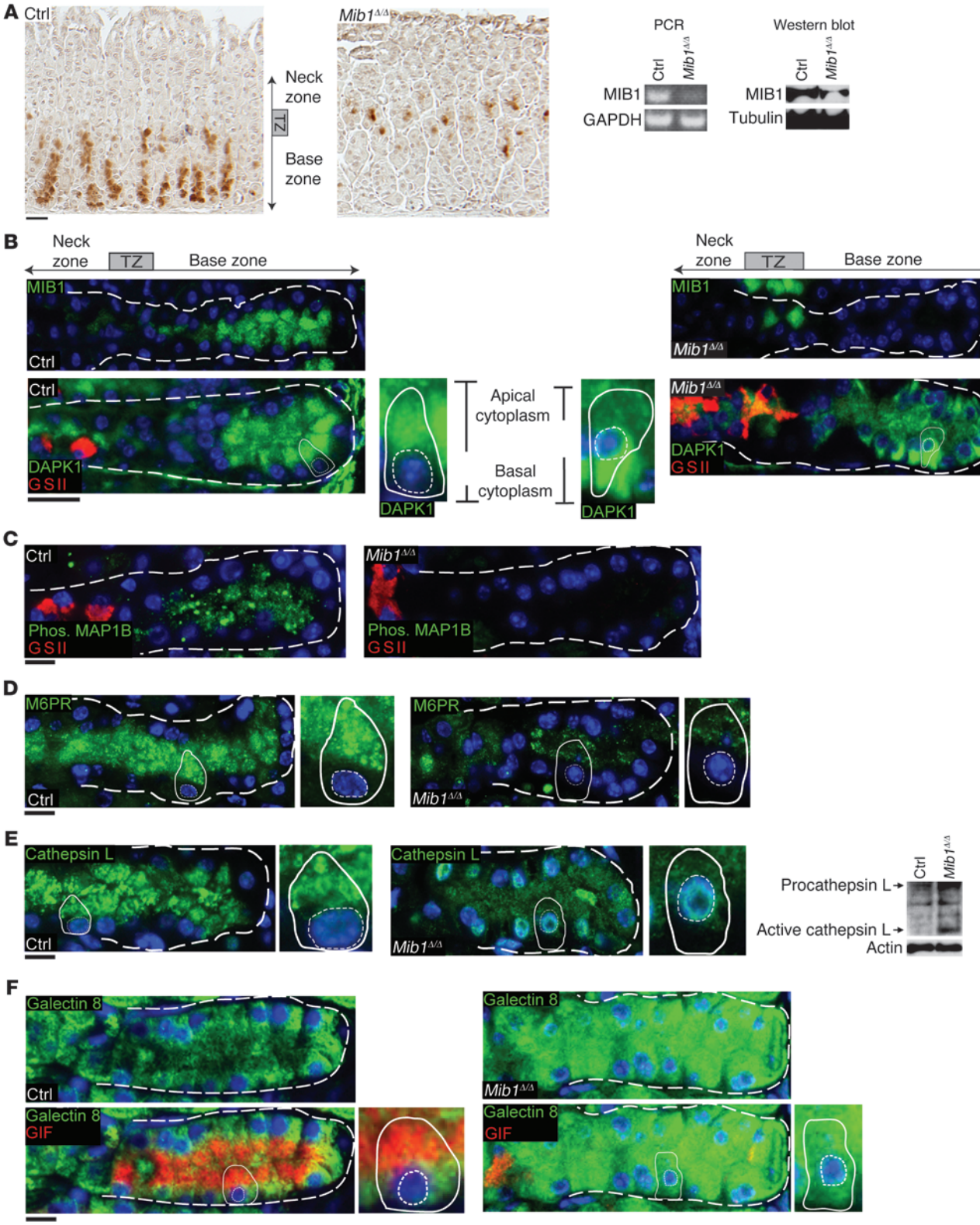
A
Ctrl
Mib1Δ/Δ
Neck zone
TZ
Base zone
PCR
Ctrl
Mib1Δ/Δ
MIB1
GAPDH
Western blot
Ctrl
Mib1Δ/Δ
MIB1
Tubulin
B
Neck zone
TZ
Base zone
MIB1
Ctrl
Mib1Δ/Δ
DAPK1
GSII
Apical cytoplasm
Basal cytoplasm
C
Phos. MAP1B
GSII
D
M6PR
E
Cathepsin L
Procathepsin L
Active cathepsin L
Actin
F
Galectin 8
GIF

Figure 3
MIB1 maintains apical compartment physiology by regulating the subcellular localization of DAPK1. (**A**) Immunohistochemistry using anti-MIB1 antibodies was performed on stomach sections from *Mib1*$^{\Delta/\Delta}$ and control (Ctrl) mice 2 weeks after initiation of tamoxifen treatment. Neck, transition, and base zones are indicated. PCR analysis of MIB1 transcript levels and Western blot analysis of MIB1 protein levels in *Mib1*$^{\Delta/\Delta}$ and control ZCs are also shown. (**B**) Fluorescent microscopy of individual gastric units (thick dashed outline) from *Mib1*$^{\Delta/\Delta}$ and control mice, 2 weeks after tamoxifen treatment, stained for MIB1 (green; top) and with GSII and DAPK1 (red and green, respectively; bottom). Enlarged views (×1.5-fold) of representative ZCs (solid outline) are shown in the insets. Thin dashed outlines denote nuclei (Hoechst, blue). Note the basal subnuclear distribution of DAPK1 in *Mib1*$^{\Delta/\Delta}$ ZCs compared with the apical localization in control mice. (**C**) Gastric units stained for GSII (red) and phosphorylated MAP1B (green). (**D** and **E**) Gastric units stained for CI-M6PR (**D**; green) or for cathepsin L (**E**; green). Enlarged views (×1.5-fold) of representative ZCs are shown in the insets. Western blot for pro–cathepsin L and activated cathepsin L is also shown in **E**. (**F**) Gastric units stained for galectin 8 (green; top) and with galectin 8 and GIF (green and red, respectively; bottom). Enlarged views (×1.5-fold) of representative ZCs are shown in the insets. Note the accumulation of galectin 8 in the apical compartment of *Mib1*$^{\Delta/\Delta}$ ZCs. Scale bars: 10 μm (**C**–**F**); 20 μm (**B**); 40 μm (**A**).

MIST1 regulates transcription of its target genes in part through its binding of a particular E-box, CATATG, frequently located within several kilobases of the end of the first exon (57, 58). Bioinformatic scanning for conserved CATATG E-boxes showed dramatic multispecies conservation of a site within 1 kb of the first intron of the *MIB1* gene (Figure 4C). We further confirmed *MIB1* as a direct MIST1 target via binding to the conserved E-box by performing ChIP on the human gastric cancer cell line HGC-27 after transient transfection of a MIST1 expression plasmid (7). Primers flanking the conserved CATATG site generated amplicons in the MIST1-immunoprecipitated genomic fragments with greater efficacy than in preimmune control–precipitated DNA, whereas primers for control regions without a CATATG sequence within 500 bp generated no amplicon (Figure 4C).

Along with ZCs, MIST1 is expressed during the terminal differentiation of several highly specialized, high-capacity secretory cell lineages in mammals (59). MIB1 was expressed in a MIST1-dependent fashion in pancreatic acinar cells, as shown by IF (Supplemental Figure 3A), and the MIST1 binding site we detected in gastric cells was also detected in pancreatic ChIP sequencing experiments (S.F. Konieczny, unpublished observations, and ref. 60). Furthermore, gene array analysis of pancreas wild-type and *Mist1*$^{-/-}$ mice showed a dramatic decrease in MIB1 gene expression (60). Interestingly, MIB1 gene expression was rescued to wild-type levels in *Mist1*$^{-/-}$ pancreatic acinar cells upon forced expression of myc-tagged MIST1 (Supplemental Figure 3A). MIB1 expression was also induced as B cells matured into antibody-secreting plasma cells and began to express MIST1 (Supplemental Figure 3B and ref. 61), and increased plasma cell MIB1 expression does not occur in *Mist1*$^{-/-}$ mice (59).

Apical compartment physiology is disrupted in the absence of MIST1. We next reasoned that, if MIST1 regulation of MIB1 is an important aspect of ZC maturation, loss of MIST1 should cause an apical compartment phenotype similar to that seen in the absence of MIB1. As in *Mib1*$^{\Delta/\Delta}$ ZCs, DAPK1 protein was mislocalized to the basal cytoplasm in *Mist1*-deficient ZCs (Figure 4D). IP from stomachs using anti-DAPK1 showed considerable association of DAPK1 and MIB1, and the abundance of DAPK1 immunoprecipitatable by MIB1 was greatly decreased in the absence of MIST1 (Figure 4D). Thus, DAPK1 localization and its ability to interact with its subcellular localizer MIB1 depended on MIST1. Other effects of the loss of MIB1 were also recapitulated by loss of MIST1: apical MAP1B was not phosphorylated in *Mist1*$^{-/-}$ ZCs, and CI-M6PR as well as cathepsin L vesicles were aberrantly trafficked (Figure 4, E and F).

We next sought to determine the potential physiological purpose of the MIST1-MIB1-DAPK1 control of ZC apical expansion. The primary purpose of ZCs is to store and secrete digestive enzymes in a regulated fashion. We reasoned that dysregulation of the vesicular compartment that has been shown to regulate secretory granule maturation would lead to disruption of ZC secretory granules. Consistent with that hypothesis, IF and Western blot analyses showed that *Mib1*-null ZCs had dramatically reduced levels of 2 proteins stored and secreted in their apical secretory granules: gastric intrinsic factor (GIF) and pepsinogen C (PGC) (Figure 5, A and B). Loss of MIB1 alone was sufficient to phenocopy the secretory granule loss characteristic of the *Mist*$^{-/-}$ ZC phenotype (16). Notably, MIB1-expressing transition cells unaffected by *Mist1*^{CreERT}-mediated deletion of *Mib1* showed abundant secretory granules filled with GIF and PGC (Figure 5, A and B), consistent with zymogenic secretory granule dependence on MIB1 and serving as an internal control highlighting the substantial depletion of granules in mature ZCs lacking MIB1.

To further characterize the defect in the granules in *Mib1*-null ZCs, we performed transmission electron microscopy (TEM). Mature zymogenic granules can be recognized by their relative electron density, which correlates with the increased packing of secretory contents. Consistent with previous reports (16, 62), wild-type ZC granules were mostly mature, although occasional granules had a more electron-lucent immature phenotype (Figure 5C, arrowheads). In all *Mib1*$^{\Delta/\Delta}$ ZCs examined, all the secretory granules were electron lucent (Figure 5C), indicative of a substantial defect in secretory granule maturation in the absence of MIB1.

To test the physiological effects of MIB1-dependent apical vesicle trafficking in ZCs, the total enzymatic activity of pepsin from wild-type and *Mib1*$^{\Delta/\Delta}$ mice was determined using a modified hemoglobin proteolysis assay, first described in 1932 by Anson and Mirsky (63). The enzymatic activity of pepsin in whole stomach was significantly reduced in *Mib1*$^{\Delta/\Delta}$ mice (Figure 5D). The magnitude of reduction was within the range seen in previous reports of decreased pepsin activity in humans during gastric atrophy and progression to gastric cancer (64).

As described above, expansion of the apical compartment and the increase in digestive enzyme–secretory vesicles depended on migration of the nucleus to the basal cytoplasm of ZCs. In *Mib1*$^{\Delta/\Delta}$ ZCs, nuclear localization — as defined by the ratio of the distance from the nucleus to the apex (marked by the tight junction protein ZO-1) to the distance from the nucleus to the basement membrane (marked by the integrin CD49f) — was significantly decreased compared with wild-type ZCs (1.2 ± 0.1 vs. 6.5 ± 0.2, $P < 0.0001$; Figure 5E).

MIB1 expression is lost in mouse and human gastric SPEM. In both mice and humans, loss (atrophy) of parietal cells causes dramatic changes in ZCs (7, 9, 10, 15, 16). When parietal cells are killed with toxins like high doses of tamoxifen in mice, ZCs decrease expression of MIST1 as they undergo SPEM, which is characterized by reexpression of neck cell markers like GSII and TFF2 and, eventu-

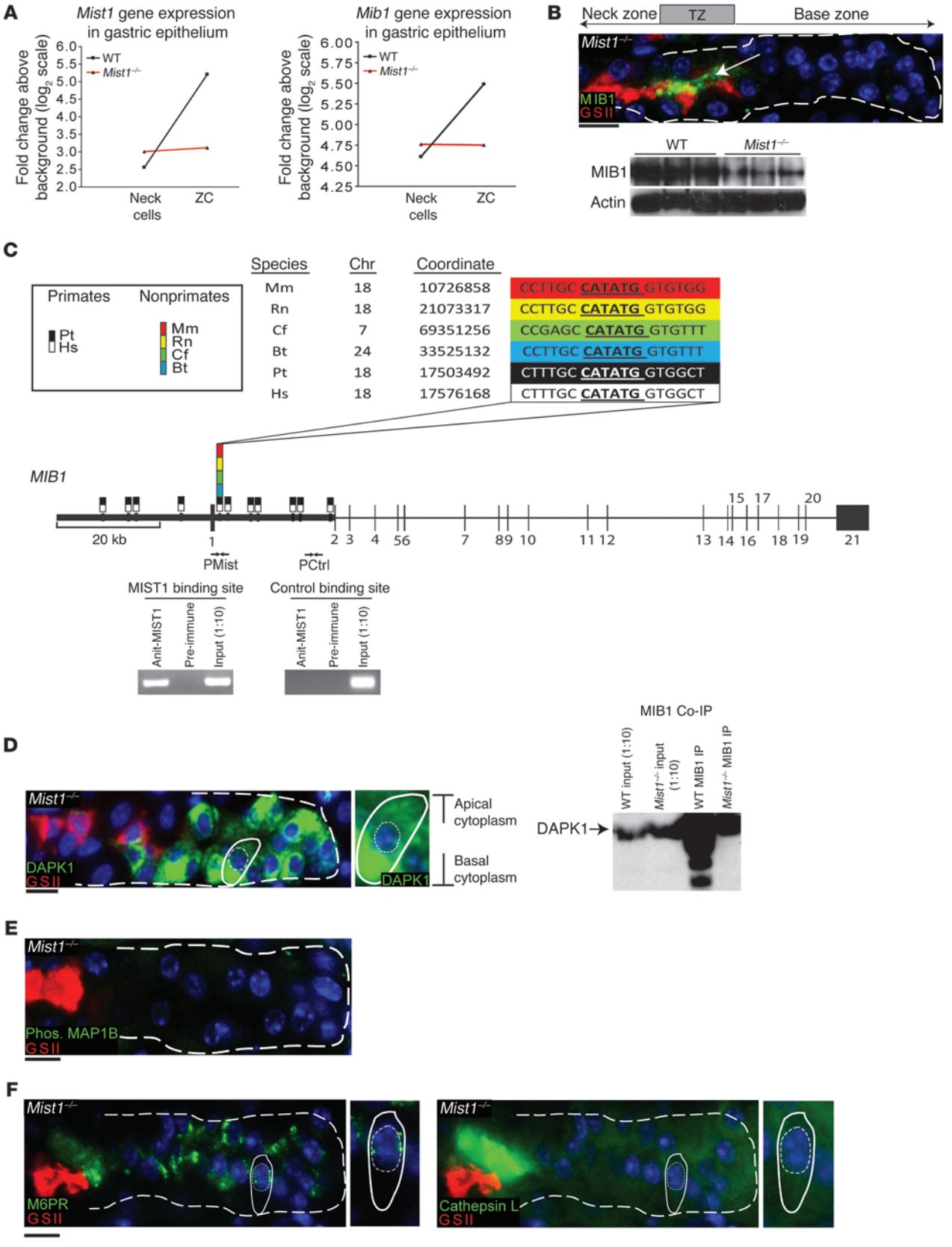
A
Mist1 gene expression in gastric epithelium
Fold change above background (log2 scale)
WT
Mist1−/−
Neck cells
ZC
Mib1 gene expression in gastric epithelium
B
Neck zone
TZ
Base zone
Mist1−/−
MIB1
GSII
WT
Mist1−/−
MIB1
Actin
C
Primates
Nonprimates
Pt
Hs
Mm
Rn
Cf
Bt
Species
Chr
Coordinate
Mm 18 10726858 CCTTGC CATATG GTGTGG
Rn 18 21073317 CCTTGC CATATG GTGTGG
Cf 7 69351256 CCGAGC CATATG GTGTTT
Bt 24 33525132 CCTTGC CATATG GTGTTT
Pt 18 17503492 CTTTGC CATATG GTGGCT
Hs 18 17576168 CTTTGC CATATG GTGGCT
MIB1
20 kb
PMist
PCtrl
MIST1 binding site
Control binding site
Anit-MIST1
Pre-immune
Input (1:10)
D
Mist1−/−
DAPK1
GSII
Apical cytoplasm
Basal cytoplasm
MIB1 Co-IP
WT input (1:10)
Mist1−/− input (1:10)
WT MIB1 IP
Mist1−/− MIB1 IP
DAPK1
E
Mist1−/−
Phos. MAP1B
GSII
F
Mist1−/−
M6PR
GSII
Cathepsin L

Figure 4
MIST1 regulates MIB1 expression during ZC differentiation. (**A**) Microarray analysis of *Mist1* and *Mib1* gene expression from isolated populations of neck cells and ZCs from wild-type and *Mist1*$^{-/-}$ mice. (**B**) *Mist1*$^{-/-}$ gastric unit (thick dashed outline) stained for GSII (red) and MIB1 (green). MIB1 was expressed in the transition zone (white arrow). Western blot of MIB1 protein levels in wild-type and *Mist1*$^{-/-}$ whole stomach corpus is also shown. (**C**) The human *MIB1* gene, represented to scale, with numbered exons as vertical lines. Note the dramatic conservation of the CATATG sequence, located within the first 1 kb of the end of the first exon, across multiple mammalian species. Also shown are gel electrophoresis images of PCR amplicons from ChIP experiments using anti-MIST1 antibody in HGC-27 cells followed by primers as indicated (see Methods). (**D**) *Mist1*$^{-/-}$ gastric unit stained for GSII (red) and DAPK1 (green). Thin dashed outlines denote nuclei (Hoechst, blue). Enlarged view (×1.5-fold) of a representative ZC (solid outline) is shown in the inset. Western blotting of MIB1 immunoprecipitates from wild-type and *Mist1*$^{-/-}$ mice for DAPK1 is also shown. (**E**) *Mist1*$^{-/-}$ gastric unit stained for GSII (red) and phosphorylated MAP1B (green). (**F**) *Mist1*$^{-/-}$ gastric unit stained for GSII (red) and for CI-M6PR (green; top) or cathepsin L (green; bottom). Enlarged views (×1.5-fold) of representative ZCs are shown in the insets. Scale bars: 10 μm (**E** and **F**); 20 μm (**B** and **D**).

ally, reentry into the cell cycle (65). In humans showing features of early SPEM, there is loss of MIST1 and equivalent cellular changes (15). We reasoned that loss of MIST1 would lead to loss of MIB1, which might affect the ZC apical secretory apparatus. Thus, we induced SPEM by killing parietal cells with 3 consecutive injections of high-dose tamoxifen (5 mg/20 g BW; Figure 6A and ref. 65). Figure 6B depicts the expression of MIST1, MIB1, and gastric epithelial cell lineage markers relative to onset and recovery from metaplasia in this system. Vehicle-treated mice showed normal development patterns of neck cells (GSII, red stain) to ZCs, with expression of MIST1 (green nuclear stain; white arrows) and MIB1 (green cytoplasmic stain) restricted to the ZCs in the base of the gastric unit, where levels of digestive enzymes (PGC, purple stain) were highest. In contrast, by the last day of toxic-dose tamoxifen treatment (i.e., day 3), expression of the neck cell marker GSII was detected in ZCs (pathognomonic for SPEM onset, which is defined by reexpression of neck cell markers like TFF2 and GSII in ZCs; ref. 15), while MIST1 levels were mostly undetectable (Figure 6A).

Metaplastic glands at this time point showed a mosaic pattern of MIB1 expression: each cell had MIB1 levels that correlated positively with expression of the digestive enzyme PGC and negatively with the neck cell marker GSII on a per-cell basis. The photomicrograph in Figure 6C is representative of the pattern we quantified by digitizing MFI in cytoplasms of all basal cells of the neck cell–ZC lineage. Next, we binned cells according to degree of MIB1 staining: cells ≥70% of maximal normalized MFI in a field were scored as 2, those ≤ 30% of maximal MFI were scored as 0, and the midrange cells received a score of 1. Quantification of individual cells in the base with differing levels of MIB1 (n = 50 cells) showed that cells with high MIB1 expression had the highest levels of PGC and almost no GSII (Figure 6C). Detectable GSII occurred only in cells with lower MIB1 expression, which also correlated with decreased PGC. We interpret cells with this intermediate MIB1 immunostaining to be hybrid cells, transitioning into SPEM. Cells with near-baseline MIB1 had low but detectable levels of PGC and showed high levels of GSII, consistent with a full SPEM phenotype. Cells at day 3 that, like normal MIB1-expressing ZCs, were not yet reexpressing the epitope for GSII also maintained DAPK1 and had phosphorylated MAP1B (Supplemental Figure 4).

Thus, MIB1 expression began to decrease during onset of metaplasia, consistent with its regulation by MIST1, which is also lost with metaplasia (15). By 7 days, gastric units had undergone complete metaplastic transformation, as indicated by the presence of GSII labeling throughout the base zone, a complete loss of MIST1, and a 78% reduction in PGC levels (Figure 6B). MIB1 expression was entirely lost in the metaplastic ZCs at this time point. As expected, DAPK1 could be found only in the basal portion of the metaplastic ZCs, and phosphorylation of MAP1B was abrogated (Supplemental Figure 4). In this metaplasia model, there is complete recovery of gastric unit differentiation within 2–3 weeks (65). Accordingly, mice at 21 days after treatment displayed recovery in the cellular and molecular architecture of the base (Figure 6B). During recovery, those cells with normal morphology, including expanded apical compartments with normal DAPK1 localization and MAP1B phosphorylation, showed reexpression of both MIST1 and MIB1, which suggests that reexpression is concomitant with recovery of the ZC lineage.

Tamoxifen-induced SPEM mimics *Helicobacter pylori*–induced SPEM; accordingly, we analyzed the base of gastric corpus units in 5 mice infected with a *CagA*$^{+}$ strain of *Helicobacter* PMSS1 8 weeks after infection. Treatment caused parietal cell atrophy and SPEM in multiple regions throughout most of the corpus. Supplemental Figure 5 shows a representative region in which a few residual normal units with MIB1-positive ZCs were preserved; note that those cells did not show labeling with GSII, whereas other gastric units throughout the corpus showed SPEM with GSII-labeled, MIB1-negative cells.

Our analysis of the time course and progression of SPEM in mice indicated that cells transitioning to SPEM progress first through a stage equivalent to that seen in our *Mib1*$^{\Delta/\Delta}$ mice, in which MIB1 is lost, and loss of the secretory vesicle apparatus leads to decreased storage of cytoplasmic PGC, but markers of neck cells are not expressed. Note that in Figure 6C, only cells without MIB1 ("0" cells) showed GSII, and those cells had diffuse, reduced PGC, whereas transitional cells with reduced MIB1 ("1" cells) maintained PGC without GSII, which suggests that MIB1 levels must drop below a critical level before the apparatus for high-capacity secretory vesicle packaging is dismantled. Expression of high levels of MIB1 was nearly exclusive of detectable GSII, which suggests that reduced MIB1 and loss of apical secretory architecture normally occur before reexpression of mucous neck cell markers in ZCs, the pattern diagnostic of SPEM.

Parietal cell atrophy in humans also correlates with loss of MIST1 in ZCs. Thus, we next sought to determine whether loss of MIB1 and downscaling of large apical PGC granules also represented a heretofore-undiscovered initial phase of SPEM in humans. We analyzed a series of 62 routine gastric biopsies and resections (Table 2) from multiple institutions in 2 different nations (15). Using MIB1 and GSII labeling, we identified those specimens with regions characterized by "hybrid," or early, SPEM with low to absent MIB1 and moderate GSII; Figure 7A shows a representative field from 1 such specimen. This specimen also showed a region with normal neck cell–to–ZC differentiation (Figure 7A, white arrows), demonstrating that in humans, as in mice, levels of MIB1 increased apically as ZCs migrated toward the base of the gastric unit. A region of mature SPEM, with high basal GSII and no MIB1, was also observed (Figure 7A, yellow

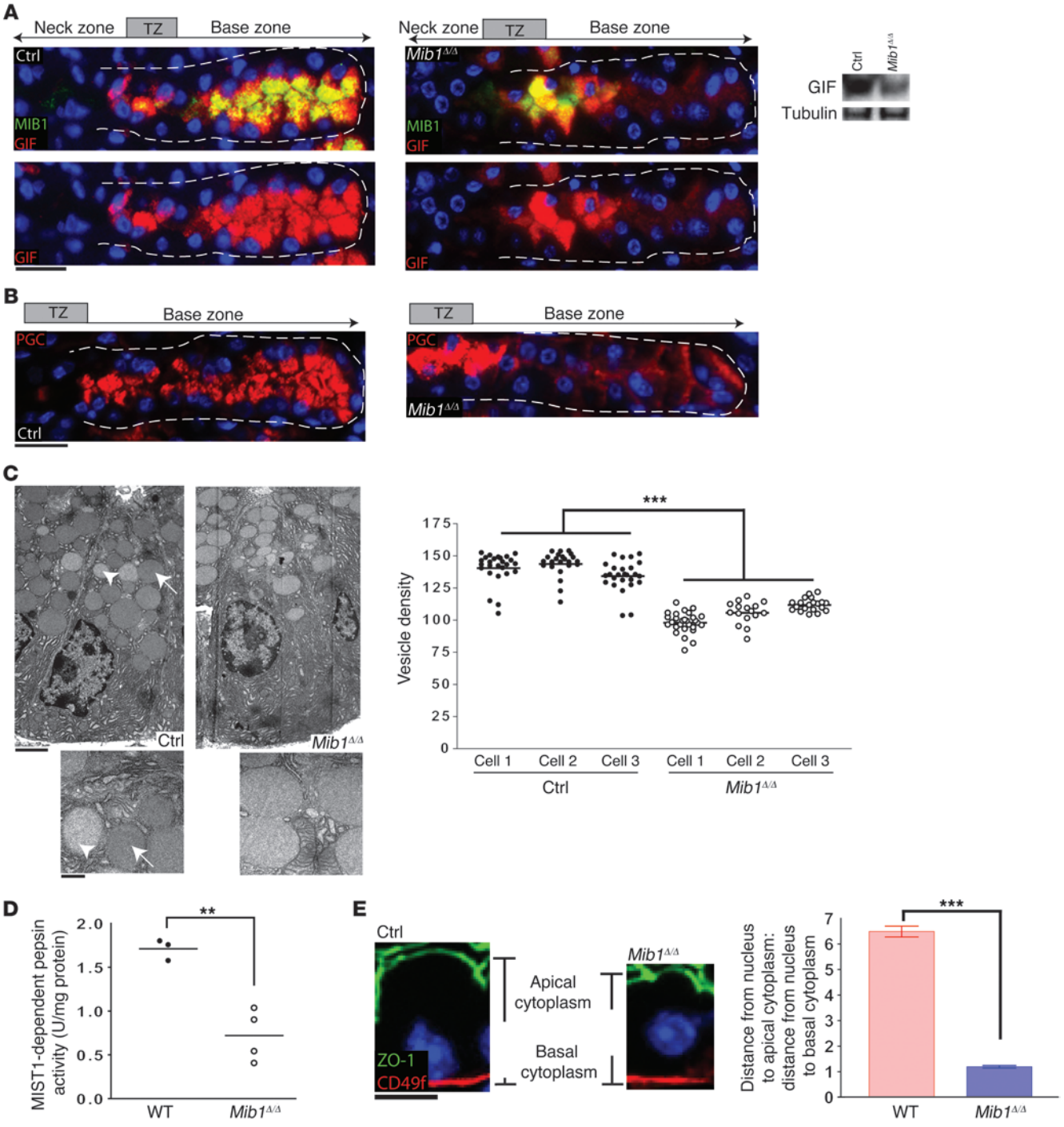

Figure 5

Disruption of apical compartment physiology in ZCs decreases the levels and enzymatic activity of digestive enzymes. (**A**) Fluorescent microscopy of individual gastric units (dashed outline) from *Mib1*$^{\Delta/\Delta}$ and control mice 2 weeks after tamoxifen treatment stained for MIB1 and GIF (green and red, respectively; top) or with GIF alone (red; bottom). Note that GIF accumulated only in the cells migrating from the neck zone with a full complement of MIB1. (**B**) Gastric units from *Mib1*$^{\Delta/\Delta}$ and control mice 2 weeks after tamoxifen treatment stained for PGC (red). Note the accumulation only in *Mib1*$^{\Delta/\Delta}$ transition cells. (**C**) TEM images of individual ZCs from *Mib1*$^{\Delta/\Delta}$ and control mice and higher-magnification views of secretory granules (insets). Scatter plots of electron density of each granule from 3 different cells per genotype are also shown. Each data point represents an individual granule within that cell. (**D**) Quantification of pepsin activity in wild-type and *Mib1*$^{\Delta/\Delta}$ mice relative to pepsin activity in *Mist1*$^{-/-}$ mice showed nearly abrogated storage of pepsinogen granules in mature ZCs. (**E**) Gastric ZCs stained for ZO-1 (green) and integrin CD49f (red). Cells are shown en face to demonstrate that cell height was consistent and parallel to cell base. Graphical representation of the ratio of the distance from nucleus to luminal apex to the distance between nucleus and cytoplasm for each group (n = 50 cells) is also shown. Scale bars: 500 nm (**C**, insets); 2 μm (**E**); 10 μm (**C**); 20 μm (**A** and **B**). Data represent mean ± SEM. $^{**}P < 0.01$; $^{***}P < 0.0001$.

outline). We analyzed all 18 specimens that had SPEM using the same MIB1 binning system we developed in mice. Regions of hybrid SPEM were relatively common, as 1 in 5 basal glands with SPEM had some features of hybrid SPEM (i.e., detectable MIB1 and low to absent GSII; Figure 7, A–C). Quantification of these regions showed that in humans, as in mice, cells with high levels of MIB1 (expression score 2) also expressed high levels of PGC while maintaining near-undetectable levels of GSII, and cells with low MIB1 levels (expression score 0) had decreased PGC stores and fully reexpressed the epitope for GSII (Figure 7D), indicative of SPEM. Figure 7C depicts a representative confocal image where transitional phenotypes could be seen in adjacent cells, highlighting transitional phenotypes between normal ZCs and SPEM in an individual unit. Note that wherever there was residual MIB1 ("2" cell, white outline), PGC expression was stronger and packaged into large apical secretory vesicles; where MIB1 was undetectable, PGC was diffuse, in smaller vesicles, or nearly undetectable ("0" cell, yellow outline). Overall, the results indicated that in humans, as in mice, substantially decreased expression of MIB1 (presumably secondary to loss of MIST1) represents the first detectable morphological change in cells transitioning to SPEM, occurring before reexpression of mucous neck cell markers.

SPEM often occurs with the other predominate type of metaplasia induced by parietal cell death, intestinal metaplasia, which is characterized by ectopic formation of intestinal epithelium (goblet cells and brush border–expressing enterocytes) and expression of the transcription factor CDX2 (15). Of the specimens we examined, 26 showed characteristics of intestinal metaplasia. MIB1 expression in these lesions was consistently low to moderate (expression score 1), but not absent (data not shown).

Given that MIB1 expression appeared to be the earliest change in ZCs after parietal cell atrophy and that gastric cancer in general occurs only in the setting of such atrophic/metaplastic changes, we hypothesized that MIB1 would not be expressed in gastric adenocarcinoma. We examined a limited cohort of 15 dysplastic and carcinomatous lesions for MIB1 expression (Table 2). There was no detectable expression of MIB1 in the dysplastic lesions, regardless of grade of dysplasia (Supplemental Figure 6A). We noted focal expression of MIB1 in 4 of 5 adenocarcinomas exhibiting signet ring morphology (Supplemental Figure 6B). The invasive adenocarcinomas with intestinal differentiation in the cohort we immunostained were uniformly MIB1 negative (Supplemental Figure 6C).

Discussion

Here, we addressed the central question of how the temporal regulation of a single gene can control specific subcellular morphology and function in a polarized epithelium. We present evidence that many aspects of the apical secretory compartment expansion that occurs in gastric ZCs are regulated at the transcriptional level by MIST1-dependent maintenance of a specific cellular effector, MIB1. Our data showed that MIB1 and DAPK1 formed a molecular complex in the apical membrane compartment during ZC maturation. Conditional knockout of *Mib1* in ZCs revealed that MIB1 was necessary for the apical localization of DAPK1. Mislocalization of DAPK1 to the basal cytoplasm caused loss of MAP1B phosphorylation and a significant defect in apical membrane trafficking and secretory granules. Collectively, these data suggest that MIB1 and DAPK1 operate as part of a signaling complex that directs the changes in apical cell structure, polarization, and endolysosomal vesicle compartmentalization as neck cells transform into ZCs. Ultimately, all of this coordination of apical protein events depended on MIST1's regulation of MIB1 at the transcriptional level.

The expansion and maturation of the apical compartment appear to be critical for secretory cell function, as loss of MIST1 and/or MIB1 caused profound maturation defects in secretory granules. Within the ZC apical cytoplasm, secretory proteins are being packaged in secretory granules for delivery to the luminal apex. Vesicles containing lysosomal hydrolases and proprotein convertases are sorted and trafficked to lysosomes in the basal cytoplasm to multivesicular or recycling endosomes as part of signaling networks and in and out of the secretory granules themselves, a process that is key to the maturation/processing of their cargo (66–69). Microtubules are the principal conduit for cellular vesicular trafficking (33, 34), and ZCs construct an elaborate network of microtubules in the apical membrane compartment. We demonstrated that the segregation of these vesicle compartments on microtubules was regulated, in part, by a signal transduction pathway that involved the phosphorylation of MAP1B by DAPK1 that was maintained by MIB1. MAP1B is a key target of DAPK1 (46). DAPK1 also plays a key role in the regulation of cell morphology by bridging membrane proteins with the cytoskeleton (46, 70–72). Finally, unbiased loss-of-function studies have shown that DAPK1 is required specifically for proper subcellular localization of late/recycling endosomes (72), the vesicular compartment expanded in the apex of maturing ZCs, as described above. These molecular events are necessary for ZCs to maintain their mature phenotype and, subsequently, their loss leads to a deficiency in mature (i.e., digestive enzyme–packed) secretory granules.

Expression of *Mib1* is significantly increased as neck cells transition to ZCs. 2 principal mechanisms have been described for MIB1 function: activation of Notch signaling though the ubiquitination and endocytosis of the Notch ligands Delta and Jagged (19, 24), and regulation of DAPK1 during apoptosis (21, 22). There is no documented role for Notch in ZC homeostasis, and we observed no changes in Notch-regulated genes during neck cell–to–ZC transition or in the absence of MIST1/MIB1. Rather, consistent with previously published data (56), we detected Notch pathway activity only in the isthmal region, where the corpus stem cell resides; this localization did not change when MIB1 was lost in ZCs (56). Moreover, the same study showed that there was no effect on the ZC lineage, or parietal cell lineage, in adult mice treated with the known Notch antagonist dibenzazepine (56). On the other hand, we here demonstrated in gastric ZCs: (a) a direct interaction between MIB1 and DAPK1; (b) that DAPK1 was ubiquitinated and ubiquitination was attenuated in the absence of MIB1; and (c) that apical localization of DAPK1 also depended on MIB1. Our studies are the first to demonstrate that MIB1 functions upstream of DAPK1 to regulate a subcellular compartment in mature, fully differentiated cells.

MIB1 target specificity and, thus, its molecular function may vary at different points in development. Indeed, recent studies have indicated that MIB1 can regulate morphogenesis of postmitotic neurons by interacting with proteins involved in the maintenance of secretory vesicle transport, cytoskeletal rearrangement, and cell adhesion (51). Collectively, these data suggest that MIB1 can function on 2 levels: during cell fate specification, and during maturation of terminally differentiated cells. Our current data highlight the importance of MIB1 in maintaining cell maturation. After we induced loss of *Mib1* expression in mature ZCs, MIB1 protein expression was consequently lost, its target proteins

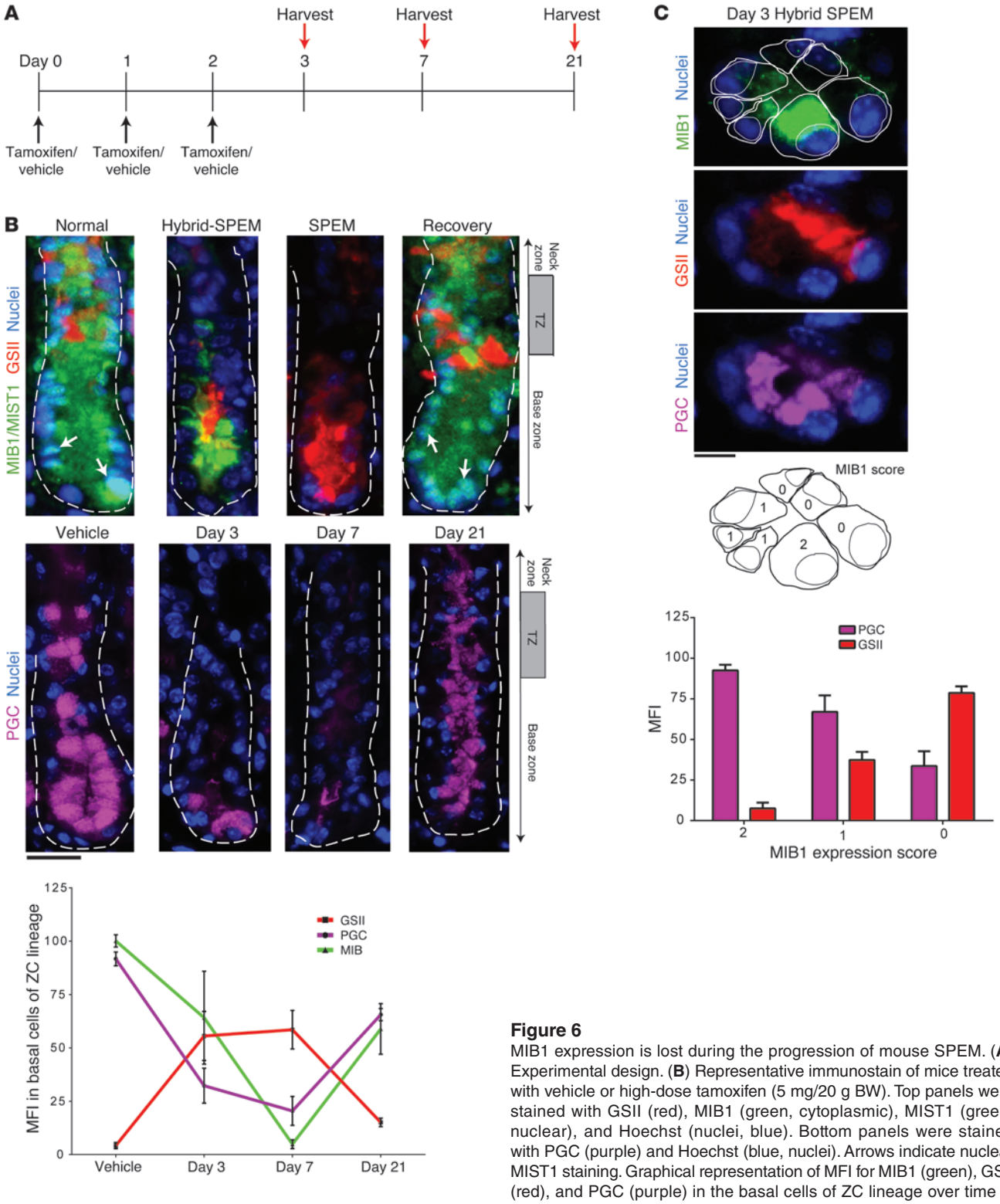

Figure 6

MIB1 expression is lost during the progression of mouse SPEM. (**A**) Experimental design. (**B**) Representative immunostain of mice treated with vehicle or high-dose tamoxifen (5 mg/20 g BW). Top panels were stained with GSII (red), MIB1 (green, cytoplasmic), MIST1 (green, nuclear), and Hoechst (nuclei, blue). Bottom panels were stained with PGC (purple) and Hoechst (blue, nuclei). Arrows indicate nuclear MIST1 staining. Graphical representation of MFI for MIB1 (green), GSII (red), and PGC (purple) in the basal cells of ZC lineage over time is also shown. (**C**) Representative immunostain of hybrid SPEM lesion at day 3 after tamoxifen treatment stained with MIB1 (green; top), GSII (red; middle), and PGC (purple; bottom). Individual cells (outlines) were assigned a MIB1 expression score: 2, high; 1, intermediate; 0, low. Graphical representation of the correlation of MIB1 expression score and MFI for PGC and GSII in individual cells is also shown. Scale bars: 5 μm (**C**); 20 μm (**B**). Data represent mean ± SD.

Table 2
Summary of MIB1 expression in patient samples

	Total incidence	Predominant MIB1 expression score		
		0	1	2
Normal	11	0	0	11
SPEM[A]	18	18	0	0
Intestinal metaplasia	26	0	26	0
Dysplasia	4	4	0	0
Cancer (diffuse type)	5	1	4	0
Cancer (intestinal adenocarcinoma)	5	5	0	0

n = 28 (Nicaragua); 34 (United States). [A]Excludes regions of hybrid SPEM analyzed in Figure 7.

began to accumulate in the wrong compartment, and cell function was abrogated. Thus, *Mib1* expression is necessary throughout the lifespan of the mature secretory cell.

The mechanisms that control *Mib1* expression had not previously been reported. Here, we revealed that *Mib1* is a direct transcriptional target of MIST1. MIST1 is a developmentally regulated transcription factor that does not specify cell fate, but rather regulates the development of secretory cell structure and function (1). Our data suggest that MIST1 regulation of *Mib1* may be generally conserved, as we have identified multiple secretory cell lineages of diverse origin — plasma cells (59) as well as gastric ZCs and pancreatic acinar cells (present study) — in which MIST1 is able to scale the levels of *Mib1* transcription. While the scaling of *Mib1* expression in stomach is regulated by MIST1, our data suggest that its transcription is initiated upstream of MIST1, possibly by another lineage-specific transcription factor, because expression of MIB1 in cells transitioning between the neck and base was maintained even in the absence of MIST1.

Stomach cancer is the fourth most common and second most fatal malignancy worldwide; however, our understanding of the molecular and morphological progressions that cause this malignancy is limited (12–14). During SPEM-type metaplasia in the stomach, ZCs reexpress markers of their progenitor mucous neck cell phase and reenter the cell cycle, increasing the risk for subsequent dysplasia and carcinoma by mechanisms that remain poorly understood (15, 73). Such changes in cell morphology are common in carcinogenesis and an area of active research (7, 9, 15, 53). We have previously shown that MIST1 expression is almost universally lost in all gastric carcinomas (15).

Our present data allow us to speculate about the molecular mechanisms underlying the transition of ZCs into SPEM cells. Using doses of tamoxifen that induce near-synchronous death of parietal cells, we followed the sequential response of ZCs, which began to lose MIB1 expression within 3 days. Concomitant with or slightly after the loss of MIB1, there was loss of densely packed apical secretory granules, as evidenced by dispersal of PGC immunolabeling from large, densely packed granules. Reexpression of the neck cell marker GSII was almost never seen in cells expressing detectable MIB1, which indicates that loss of MIB1 and dismantling of the apical secretory apparatus occur before neck cell marker reexpression. In mice infected with *H. pylori* and in multiple human stomach specimens, in regions transitional between complete SPEM and normal morphology, we saw the same morphological patterns: namely, MIB1 and GSII were mutually exclusive, and MIB1 expression was highly positively correlated with normal apical PGC granular content.

We speculate that dismantling of the apical secretory apparatus, which could be identified by loss of MIB1 labeling in ZCs, is a distinct step in metaplasia that occurs before the changes currently used to diagnose appearance of SPEM (i.e., reexpression of neck cell markers). Given that loss of MIB1 alone in $Mib1^{\Delta/\Delta}$ ZCs was sufficient to induce a morphology similar to this initial stage of metaplasia, with disrupted apical secretory granule packaging, and that loss of MIST1 caused loss of *Mib1*, we propose that loss of MIST1 expression is the initial molecular event that induces this first step in transition to metaplasia. Loss of MIB1 alone, however, was not sufficient to cause neck cell marker expression in ZCs. Thus, other mechanisms independent of MIB1 must induce expression of neck cell genes, which does not seem surprising, as it would not be obvious how MIB1 regulating apical cytoskeletal and trafficking machinery might affect transcription and/or translation. Although loss of MIB1 is apparently sufficient for the initial phase of SPEM, it is not clear whether MIB1 must be lost for the next phase of SPEM to occur, which is a clear avenue for future study. Dedifferentiation of MIST1-expressing cells also occurs during acinar-to-ductal metaplasia in the pancreas, which has been called the initiating event for ductal adenocarcinomas in that organ (53, 60, 74). It is interesting to speculate whether loss of MIB1-dependent apical secretory differentiation in those cells also occurs prior to the reexpression of ductal markers in a manner that parallels loss of MIB1 prior to reexpression of neck cell markers in the stomach.

Together, our results indicate a key regulatory mechanism involved both in the normal scaling up of a specific subcellular compartment required for normal physiology of exocrine secretory cells and in the scaling down of that same compartment in those same cells during pathophysiological changes. This mechanism may be conserved in a cross-species, cross-tissue fashion, providing a tool for understanding how cells in diverse environments derive their form and function throughout development.

Methods

Mice. Germline $Mist^{-/-}$ mice (75) were maintained in a specific pathogen–free barrier facility. $Mist1^{CreERT}$ mice were generated as previously described (53) and bred to $Mib1^{fl/fl}$ mice (24). $Mist1^{CreERT/+}Mib1^{fl/fl}$ mice were generated and at 6 weeks of age were given 5 consecutive intraperitoneal injections of tamoxifen (1 mg/20 g BW; Sigma-Aldrich). Deletion of *Mib1* did not lead to immediate death of ZCs, as there was no substantial difference in ZC census or apoptosis levels between control mice (i.e., tamoxifen-treated animals not expressing $Mist1^{CreERT}$) and induced *Mib1*-null mice. Control mice were $Mist1^{CreERT/+}Mib1^{fl/fl}$ mice treated with tamoxifen vehicle only or were tamoxifen-treated littermates of $Mist1^{CreERT/+}Mib1^{fl/fl}$ mice that lacked either the *Cre* allele ($Mist1^{+/+}Mib1^{fl/fl}$) or both flox inserts ($Mist1^{CreERT/+}Mib1^{+/+}$).

Patient samples. Serial sections (4–6 μm thick) obtained from paraffin-embedded tissue samples (H&E and alcian blue–periodic acid–Schiff stains) were reviewed by 2 pathologists with specific expertise in gastrointestinal diseases, and a consensus on the score for each pertinent histologic variable was reached. Diagnoses and selection of specific regions of transition among normal stomach, atrophic stomach, and intestinal metaplasia was performed by a third pathologist.

IF/cell imaging. Stomachs were prepared and stained as described previously (16). Briefly, stomachs were inflated with freshly prepared methacarn fixative and suspended in fixative for 15–30 minutes at room temperature,

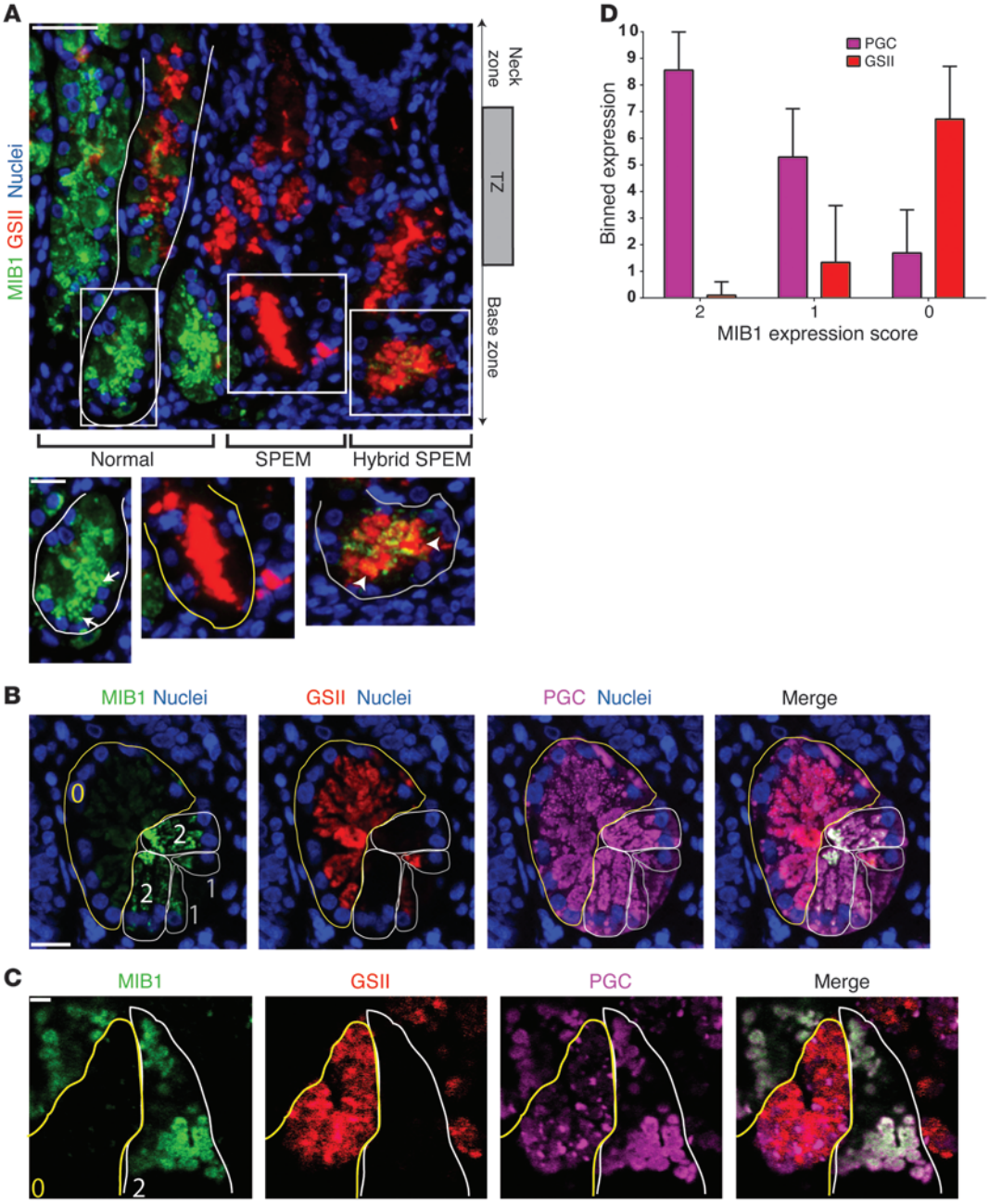

Figure 7

MIB1 in human metaplasia and cancer. (**A**) Unitary variation of MIB1 (green) and GSII (red), presenting as normal pattern, hybrid SPEM, and complete SPEM, as indicated. Normal gastric mucosa showed MIB1-positive ZCs (arrows). The hybrid SPEM region showed decreased levels of MIB1 and coexpression of GSII in the base of the gland (arrowheads). In contrast, MIB1 expression was completely lost in fully transformed SPEM (yellow outline). (**B** and **C**) Representative immunostain (**B**) and confocal imaging (**C**) of a hybrid SPEM lesion stained for MIB1 (green), GSII (red), PGC (purple), and Hoechst (blue, nuclei). Cells with MIB1 expression scores of 0 (yellow outline), 1 (gray outline), and 2 (white outline) are indicated. (**D**) Graphical representation of the correlation of MIB1 expression score and PGC and GSII expression (MFI) in individual cells. Data represent mean ± SD. Scale bars: 1 μm (**C**); 10 μm (**B**; **A**, insets); 50 μm (**A**).

followed by multiple rinses in 70% ethyl alcohol (EtOH), arrangement in 2% agar in a tissue cassette, and routine paraffin processing. Sections (5 μm) were deparaffinized and rehydrated, and then antigen retrieval was performed by boiling in 50 mM Tris-HCl, pH 9.0. Slides were blocked in 1% BSA and 0.3% Triton X-100 in PBS and then incubated in primary antibodies followed by secondary antibodies. Slides were incubated for 5 minutes in 1 μg/ml bisbenzimide (Invitrogen) prior to mounting in 1:1 glycerol-PBS. Fluorescence microscopy and imaging were performed using a Zeiss Axiovert 200 microscope with ×20 (Plan-Apochromat, 0.811 NA), ×40 (Plan-Neofluar, 0.85 NA), and ×63 (Plan-Apochromat, 1.4 NA) objectives with an Axiocam MRM camera and AxioVision software. Additional confocal microscopy and imaging were performed using a Zeiss LSM510

META microscope with ×40 (EC Plan-Neofluar, 0.7516 NA) and ×63 (Plan-Apochromat, 1.4 NA) objectives using LSM510 software.

To visualize microtubules, stomachs were flushed with PBS at 37°C, followed by 2% paraformaldehyde, 75 mM lysine, 25 mM taxol, 0.1% Triton X-100 in PBS. Sections were fixed for 20 minutes at 37°C followed by a wash with 5% sucrose in PBS at 37°C and embedded in OCT. 5-μm-thick sections were cut, rehydrated in PBS, and incubated with Alexa Fluor 488–conjugated anti–α-tubulin antibody (eBioscience).

The following primary antibodies were used for immunostaining: goat anti-human GIF (1:2,000; gift of D. Alpers, Washington University School of Medicine); sheep anti-PGC (1:10,000; Abcam); mouse anti–α-tubulin (1:500; Sigma-Aldrich); phalloidin; myosin; integrin; mouse anti–cathepsin L (1:100; Novus Biologicals); rabbit anti–CI-M6PR (1:500; gift of S. Kornfeld, Washington University School of Medicine); mouse anti-MAP1B (1:100; Sigma-Aldrich); rabbit anti–phosphorylated MAP1B (1:200; Novus Biologicals); rabbit anti-DAPK1 (1:200; Sigma-Aldrich); rabbit anti-MIB1 (1:500; Sigma-Aldrich); mouse anti–galectin 8 (1:100; Sigma-Aldrich); rabbit anti-MIST1 (1:200; ref. 15). Secondary antibodies used were Alexa Fluor 488–, 594–, and 647–conjugated donkey anti-goat, anti-rabbit, anti-sheep, and anti-mouse antibodies (1:500; Invitrogen).

IF quantification to determine cytoplasmic MFI was performed with NIH ImageJ software. MFI was determined in each cell after subtraction of background, which was determined by averaging the fluorescence signal in 5 parietal cells, which did not express any lineage marker examined, from the same gastric unit.

Apical cytoplasm measurements were performed using Image J software.

LCM and quantitative real-time PCR (qRT-PCR). Preparation of stomach frozen sections for LCM has been described previously (16). Briefly, stomachs were excised immediately after sacrifice, quickly flushed with room-temperature PBS, inflated by duodenal injection of OCT compound (Sakura Finetek), frozen in Cytocool II (Richard-Allen Scientific), and cut into serial 7-μm-thick cryosections, which were mounted on Superfrost slides (Fisher Scientific), fixed in 70% EtOH, rehydrated in nuclease-free water (nuclease-free solutions from Ambion), and then incubated in Alexa Fluor 488–conjugated *Griffonia simplicifolia* GSII (diluted 1:500 in nuclease-free water) for 15 minutes. Sections were washed in nuclease-free water and dehydrated in graded ethanol followed by xylene. ZCs were identified as corpus cells that were basal to GSII labeling and did not show the dark silhouettes and characteristic shape of parietal cells after xylene dehydration. 4 wild-type mice and 5 *Mist1*$^{-/-}$ mice were used for dissection (PixCell II LCM apparatus [7.5-μm spot diameter] and CapSure HS LCM caps; Arcturus) to generate 2 caps per mouse. RNA was purified by PicoPure kit (Arcturus), and RNA integrity was confirmed by an Agilent 2100 Bioanalyzer. qRT-PCR was performed only on RNA that had sharp 18S and 28S bands. All RNA from each cap was treated with DNase I (Invitrogen) and then reverse transcribed using the SuperScript III (Invitrogen) standard protocol (most cDNA syntheses started with 10 ng total RNA). Measurement of cDNA levels was performed by qRT-PCR using a Stratagene MX3000P detection system, and Absolute QPCR SYBR green mix (Thermo Scientific) fluorescence was used to quantify relative amplicon amounts of mouse *Mib1*, *Mist1*, and *18S* rRNA, with the following primers: *Mib1* forward, GTCATCCCAGTCTCCAGGATTCTGAA; *Mib1* reverse, GGACCAAAAGCCTAACAATCTGGGT; *Mist1* forward, TGGTGGCTAAAGCTACGTGTC; *Mist1* reverse, GACTGGGGTCTGTCAGGTGT; *18S* forward, CATTCGAACGTCTGCCCTATC; *18S* reverse, CCTGTGCCTTCCTTGGA.

Gene chips and bioinformatic analysis. Gene chip arrays used in these experiments were Affymetrix Mouse Gene 1.0ST arrays. Chip quality control and GeneChip-to-GeneChip comparisons to generate expression profiles were performed using dChip (76, 77). Cell lineage–specific profiles were generated by extracting those genes whose expression was increased in the given cell lineage relative to the other lineages, according to the following parameters: lower bound of 90% confidence, fold change ≥1.2; expression intensity difference, ≥50. Parietal cell–specific genes were derived from LCM experiments previously performed (16), and those genes were removed from the list of ZC-specific genes. Gene chips are available through GEO (accession no. GSE43441).

Conversion of cell-specific gene lists into GO distributions. Lists of cell type–specific genes for each gastric epithelial cell lineage were associated with GO terms using GOurmet Vocabulary software (29). Among those GO terms, those associated with specific subcellular domains or processes were identified and depicted in Figure 1, Table 1, and Supplemental Figure 1.

Analysis of MIB1 gene cis-regulatory elements. The ECR browser (78) was used to analyze the human genomic sequence for *MIB1* 5′ to the transcription start. Sequence was analyzed up to 50 kb or until an exon from the neighboring gene was reached. The first intron up to 50 kb was also analyzed. CATATG sequences within analyzed sequences were identified using the dreg application in the EMBOSS suite. Conservation among species aligned in the ECR browser was then determined at each of these CATATG sites.

ChIP. ChIP was performed as previously described (57). Approximately 10^8 HGC-27 cells transfected with a MIST1 expression plasmid were harvested for 1 ChIP experiment. 15 μl of MIST1 antiserum (rabbit polyclonal anti-human MIST1) or serum from the rabbit prior to immunization (preimmune control) together with protein A/G plus agarose (Santa Cruz Biotechnology) was added to the cell lysate for IP. Regular PCR and qRT-PCR were performed to assess the quantity of genomic sequences immunoprecipitated by either preimmune control or MIST1 antiserum, as well as a 1:10 dilution of the cell extract prior to IP. The following primers were used to assess IP of binding sites: MIST1 conserved site forward, CGACTCCTCCTCTTGGGAAG; MIST1 conserved site reverse, CATCTCCACAAATCCGAGGT; control site forward, GCAGGATAGCCAACCTTCAT; control site reverse, TATTATAGTCCTGGGGCAAAACA.

Western blot, qRT-PCR, and co-IP from stomach tissue. For blots, corpus tissue was homogenized in RIPA buffer using a PowerGen 700 (Fischer Scientific) with proteins separated on NuPAGE 4%–12% (Invitrogen), transferred to polyvinylidene difluoride, and detected by Immobilon chemiluminescence (Millipore). Primary antibodies were rabbit anti-MIB1 (1:1,000), rabbit anti-DAPK1 (1:1,000), goat anti-GIF (1:20,000), and goat anti-actin (1:1,000; Santa Cruz Biotechnology). Secondary antibodies were horseradish peroxidase–conjugated donkey anti-rabbit (1:2,000; Jackson ImmunoResearch) and donkey anti-goat (1:2,000; Santa Cruz Biotechnology). For qRT-PCR, total RNAs from corpus were extracted and assayed as described previously (79). Co-IP was performed using a Pierce Crosslink IP Kit (Thermo Scientific) with anti-MIB1 antibodies (Sigma-Aldrich) or anti-ubiquitin antibodies (Santa Cruz Biotechnology).

TEM. For TEM studies, stomachs were fixed, sectioned, stained, and imaged as previously described (16). Scoring of electron density was performed using Image J.

Statistics. All graphs and statistics were determined with GraphPad Prism and then visualized using Adobe Illustrator. Statistical analysis was by 2-tailed Student's *t* test. A *P* value of 0.05 or less was considered significant.

Study approval. All experiments involving animals were performed according to protocols approved by the Washington University School of Medicine Animal Studies Committee. Acquisition of human gastric pathological tissue specimens was approved by the Institutional Review Board of Washington University School of Medicine, the Comité de Bioetica of Nicaragua for Universidad Nacional Autonoma De Nicaragua — Facultad De Ceincias Medicas Managua, and the Research Ethics Board Manager for Health Sciences at the University of Toronto. Either patients provided informed consent prior to their participation, or, in some cases, tissue was from archived specimens taken for diagnosis, so informed consent

was exempted, with the exemption approved by the Institutional Review Board of Washington University.

Acknowledgments

The authors thank the Morphology Core of the Digestive Disease Research Core Center (DDRCC); Karen Green and Wandy Beatty for EM and confocal microscopy assistance; Stuart Kornfeld for sharing valuable antibodies; and Jim Skeath and Indira Mysorekar for thoughtful review of the manuscript. This work was supported by grants to J.C. Mills from the NIH (R01 DK-079798-01) and the American Cancer Society (DDC-115769) and to B.J. Capoccia from the DDRCC (P30 DK052574). The authors acknowledge Vincenza Guzzardo (University of Padua) for technical support; Reyna Victoria Palacios-Gonzalez (Hospital Salud Integral, Managua, Nicaragua) and Hala El-Zimaity (University Health Network, Toronto, Ontario, Canada) for pathological diagnoses; and Lawrence Paszat for funding and coordinating acquisition of Nicaraguan samples. Additional funding for acquisition of Nicaraguan specimens was provided by David Graham and the Texas Medical Center Digestive Diseases Center (DK56338). This work was also supported by Italian Association for Cancer research (AIRC) regional grant 2008 to M. Rugge and by NIH grants to R.M. Peek Jr. (R01 DK58587, R01 CA 77955, and P01 116037); and the Vanderbilt Digestive Disease Research Center (P30 DK 508404).

Received for publication July 9, 2012, and accepted in revised form January 17, 2013.

Address correspondence to: Jason C. Mills, Department of Medicine, Washington University School of Medicine, Box 8124, 660 S. Euclid Ave., St. Louis, Missouri 63110, USA. Phone: 314.362.4258; Fax: 314.362.7487; E-mail: jmills@wustl.edu.

1. Mills JC, Taghert PH. Scaling factors: transcription factors regulating subcellular domains. *Bioessays*. 2012;34(1):10–16.
2. Lee AH, Chu GC, Iwakoshi NN, Glimcher LH. XBP-1 is required for biogenesis of cellular secretory machinery of exocrine glands. *EMBO J*. 2005; 24(24):4368–4380.
3. Lee AH, Iwakoshi NN, Glimcher LH. XBP-1 regulates a subset of endoplasmic reticulum resident chaperone genes in the unfolded protein response. *Mol Cell Biol*. 2003;23(21):7448–7459.
4. Huh WJ, et al. XBP1 controls maturation of gastric zymogenic cells by induction of MIST1 and expansion of the rough endoplasmic reticulum. *Gastroenterology*. 2010;139(6):2038–2049.
5. Sardiello M, et al. A gene network regulating lysosomal biogenesis and function. *Science*. 2009; 325(5939):473–477.
6. Sardiello M, Ballabio A. Lysosomal enhancement: a CLEAR answer to cellular degradative needs. *Cell Cycle*. 2009;8(24):4021–4022.
7. Bredemeyer AJ, et al. The gastric epithelial progenitor cell niche and differentiation of the zymogenic (chief) cell lineage. *Dev Biol*. 2009;325(1):211–224.
8. Leys CM, et al. Expression of Pdx-1 in human gastric metaplasia and gastric adenocarcinoma. *Hum Pathol*. 2006;37(9):1162–1168.
9. Nomura S, et al. Spasmolytic polypeptide expressing metaplasia to preneoplasia in H. felis-infected mice. *Gastroenterology*. 2004;127(2):582–594.
10. Nomura S, Yamaguchi H, Ogawa M, Wang TC, Lee JR, Goldenring JR. Alterations in gastric mucosal lineages induced by acute oxyntic atrophy in wild-type and gastrin-deficient mice. *Am J Physiol Gastrointest Liver Physiol*. 2005;288(2):G362–375.
11. Nozaki K, et al. A molecular signature of gastric metaplasia arising in response to acute parietal cell loss. *Gastroenterology*. 2008;134(2):511–522.
12. Parkin DM, Bray F, Ferlay J, Pisani P. Global cancer statistics, 2002. *CA Cancer J Clin*. 2005;55(2):74–108.
13. Hisamuddin IM, Yang VW. Genetics of colorectal cancer. *MedGenMed*. 2004;6(3):13.
14. Capoccia BJ, Huh WJ, Mills JC. How form follows functional genomics: gene expression profiling gastric epithelial cells with a particular discourse on the parietal cell. *Physiol Genomics*. 2009;37(2):67–78.
15. Lennerz JK, et al. The transcription factor MIST1 is a novel human gastric chief cell marker whose expression is lost in metaplasia, dysplasia, and carcinoma. *Am J Pathol*. 2010;177(3):1514–1533.
16. Ramsey VG, Doherty JM, Chen CC, Stappenbeck TS, Konieczny SF, Mills JC. The maturation of mucus-secreting gastric epithelial progenitors into digestive-enzyme secreting zymogenic cells requires Mist1. *Development*. 2007;134(1):211–222.
17. Koo BK, et al. Mind bomb-2 is an E3 ligase for Notch ligand. *J Biol Chem*. 2005;280(23):22335–22342.
18. Haddon C, Jiang YJ, Smithers L, Lewis J. Delta-Notch signalling and the patterning of sensory cell differentiation in the zebrafish ear: evidence from the mind bomb mutant. *Development*. 1998;125(23):4637–4644.
19. Itoh M, et al. Mind bomb is a ubiquitin ligase that is essential for efficient activation of Notch signaling by Delta. *Dev Cell*. 2003;4(1):67–82.
20. Wang W, Struhl G. Distinct roles for Mind bomb, Neuralized and Epsin in mediating DSL endocytosis and signaling in Drosophila. *Development*. 2005;132(12):2883–2894.
21. Jin Y, Blue EK, Dixon S, Shao Z, Gallagher PJ. A death-associated protein kinase (DAPK)-interacting protein, DIP-1, is an E3 ubiquitin ligase that promotes tumor necrosis factor-induced apoptosis and regulates the cellular levels of DAPK. *J Biol Chem*. 2002;277(49):46980–46986.
22. Jin Y, Blue EK, Gallagher PJ. Control of death-associated protein kinase (DAPK) activity by phosphorylation and proteasomal degradation. *J Biol Chem*. 2006;281(51):39033–39040.
23. Yoon MJ, et al. Mind bomb-1 is essential for intraembryonic hematopoiesis in the aortic endothelium and the subaortic patches. *Mol Cell Biol*. 2008; 28(15):4794–4804.
24. Koo BK, et al. An obligatory role of mind bomb-1 in notch signaling of mammalian development. *PLoS One*. 2007;2(11):e1221.
25. Jeong HW, et al. Inactivation of Notch signaling in the renal collecting duct causes nephrogenic diabetes insipidus in mice. *J Clin Invest*. 2009; 119(11):3290–3300.
26. Horn S, et al. Mind bomb 1 is required for pancreatic beta-cell formation. *Proc Natl Acad Sci U S A*. 2012;109(19):7356–7361.
27. Yoon KJ, et al. Mind bomb 1-expressing intermediate progenitors generate notch signaling to maintain radial glial cells. *Neuron*. 2008;58(4):519–531.
28. Karam SM, Leblond CP. Dynamics of epithelial cells in the corpus of the mouse stomach. III. Inward migration of neck cells followed by progressive transformation into zymogenic cells. *Anat Rec*. 1993;236(2):297–313.
29. Doherty JM, Carmichael LK, Mills JC. GOurmet: a tool for quantitative comparison and visualization of gene expression profiles based on gene ontology (GO) distributions. *BMC Bioinformatics*. 2006;7:151.
30. Doherty JM, Geske MJ, Stappenbeck TS, Mills JC. Diverse adult stem cells share specific higher-order patterns of gene expression. *Stem Cells*. 2008; 26(8):2124–2130.
31. Niu MY, Mills JC, Nachmias VT. Development of polarity in human erythroleukemia cells: roles of membrane ruffling and the centrosome. *Cell Motil Cytoskeleton*. 1997;36(3):203–215.
32. Drewes G, Ebneth A, Mandelkow EM. MAPs, MARKs and microtubule dynamics. *Trends Biochem Sci*. 1998;23(8):307–311.
33. Fass E, Shvets E, Degani I, Hirschberg K, Elazar Z. Microtubules support production of starvation-induced autophagosomes but not their targeting and fusion with lysosomes. *J Biol Chem*. 2006; 281(47):36303–36316.
34. Kochl R, Hu XW, Chan EY, Tooze SA. Microtubules facilitate autophagosome formation and fusion of autophagosomes with endosomes. *Traffic*. 2006;7(2):129–145.
35. Xie R, Nguyen S, McKeehan K, Wang F, McKeehan WL, Liu L. Microtubule-associated protein 1S (MAP1S) bridges autophagic components with microtubules and mitochondria to affect autophagosomal biogenesis and degradation. *J Biol Chem*. 2011;286(12):10367–10377.
36. Dogterom M, Kerssemakers JW, Romet-Lemonne G, Janson ME. Force generation by dynamic microtubules. *Curr Opin Cell Biol*. 2005;17(1):67–74.
37. Collette J, et al. Biosynthesis and alternate targeting of the lysosomal cysteine protease cathepsin L. *Int Rev Cytol*. 2004;241:1–51.
38. Funkelstein L, Beinfeld M, Minokadeh A, Zadina J, Hook V. Unique biological function of cathepsin L in secretory vesicles for biosynthesis of neuropeptides. *Neuropeptides*. 2010;44(6):457–466.
39. Jiang L, Erickson A, Rogers J. Multivesicular bodies: a mechanism to package lytic and storage functions in one organelle? *Trends Cell Biol*. 2002;12(8):362–367.
40. Ahn K, et al. An alternate targeting pathway for procathepsin L in mouse fibroblasts. *Traffic*. 2002; 3(2):147–159.
41. Yeyeodu S, Ahn K, Madden V, Chapman R, Song L, Erickson AH. Procathepsin L self-association as a mechanism for selective secretion. *Traffic*. 2000; 1(9):724–737.
42. Mandell JW, Banker GA. Microtubule-associated proteins, phosphorylation gradients, and the establishment of neuronal polarity. *Perspect Dev Neurobiol*. 1996;4(2–3):125–135.
43. Trivedi N, Marsh P, Goold RG, Wood-Kaczmar A, Gordon-Weeks PR. Glycogen synthase kinase-3beta phosphorylation of MAP1B at Ser1260 and Thr1265 is spatially restricted to growing axons. *J Cell Sci*. 2005;118(pt 5):993–1005.
44. Del Rio JA, et al. MAP1B is required for Netrin 1 signaling in neuronal migration and axonal guidance. *Curr Biol*. 2004;14(10):840–850.
45. Avila J, Ulloa L, Diez-Guerra J, Diaz-Nido J. Role of phosphorylated MAPlB in neuritogenesis. *Cell Biol Int*. 1994;18(5):309–314.
46. Harrison B, et al. DAPK-1 binding to a linear peptide motif in MAP1B stimulates autophagy and membrane blebbing. *J Biol Chem*. 2008;

283(15):9999–10014.
47. Baumann K, Mandelkow EM, Biernat J, Piwnica-Worms H, Mandelkow E. Abnormal Alzheimer-like phosphorylation of tau-protein by cyclin-dependent kinases cdk2 and cdk5. *FEBS Lett*. 1993; 336(3):417–424.
48. Drewes G, et al. Mitogen activated protein (MAP) kinase transforms tau protein into an Alzheimer-like state. *EMBO J*. 1992;11(6):2131–2138.
49. Bialik S, Bresnick AR, Kimchi A. DAP-kinase-mediated morphological changes are localization dependent and involve myosin-II phosphorylation. *Cell Death Differ*. 2004;11(6):631–644.
50. Bingham S, Chaudhari S, Vanderlaan G, Itoh M, Chitnis A, Chandrasekhar A. Neurogenic phenotype of mind bomb mutants leads to severe patterning defects in the zebrafish hindbrain. *Dev Dyn*. 2003;228(3):451–463.
51. Choe EA, et al. Neuronal morphogenesis is regulated by the interplay between cyclin-dependent kinase 5 and the ubiquitin ligase mind bomb 1. *J Neurosci*. 2007;27(35):9503–9512.
52. Hansson EM, et al. Control of Notch-ligand endocytosis by ligand-receptor interaction. *J Cell Sci*. 2010;123(pt 17):2931–2942.
53. Shi G, et al. Loss of the acinar-restricted transcription factor Mist1 accelerates Kras-induced pancreatic intraepithelial neoplasia. *Gastroenterology*. 2009;136(4):1368–1378.
54. Thurston TL, Wandel MP, von Muhlinen N, Foeglein A, Randow F. Galectin 8 targets damaged vesicles for autophagy to defend cells against bacterial invasion. *Nature*. 2012;482(7385):414–418.
55. Goldenring JR, Nam KT, Mills JC. The origin of pre-neoplastic metaplasia in the stomach: chief cells emerge from the Mist. *Exp Cell Res*. 2011; 317(19):2759–2764.
56. Kim TH, Shivdasani RA. Notch signaling in stomach epithelial stem cell homeostasis. *J Exp Med*. 2011;208(4):677–688.
57. Tian X, et al. RAB26 and RAB3D are direct transcriptional targets of MIST1 that regulate exocrine granule maturation. *Mol Cell Biol*. 2010;30(5):1269–1284.
58. Park D, Shafer OT, Shepherd SP, Suh H, Trigg JS, Taghert PH. The Drosophila basic helix-loop-helix protein DIMMED directly activates PHM, a gene encoding a neuropeptide-amidating enzyme. *Mol Cell Biol*. 2008;28(1):410–421.
59. Capoccia BJ, Lennerz JK, Bredemeyer AJ, Klco JM, Frater JL, Mills JC. Transcription factor MIST1 in terminal differentiation of mouse and human plasma cells. *Physiol Genomics*. 2011;43(3):174–186.
60. Direnzo D, et al. Induced Mist1 expression promotes remodeling of mouse pancreatic acinar cells. *Gastroenterology*. 2012;143(2):469–480.
61. Bhattacharya D, et al. Transcriptional profiling of antigen-dependent murine B cell differentiation and memory formation. *J Immunol*. 2007; 179(10):6808–6819.
62. Johnson CL, Kowalik AS, Rajakumar N, Pin CL. Mist1 is necessary for the establishment of granule organization in serous exocrine cells of the gastrointestinal tract. *Mech Dev*. 2004;121(3):261–272.
63. Anson ML, Mirsky AE. The Estimation of Pepsin with hemoglobin. *J Gen Physiol*. 1932;16(1):59–63.
64. Miki K, et al. Potential peptic activity of pepsinogen of human gastroduodenal mucosa determined by fluorescent microassay method using succinyl albumin. *Clin Chim Acta*. 1982;121(3):337–344.
65. Huh WJ, Khurana SS, Geahlen JH, Kohli K, Waller RA, Mills JC. Tamoxifen induces rapid, reversible atrophy, and metaplasia in mouse stomach. *Gastroenterology*. 2011;142(1):21–24.e7.
66. Arvan P, Castle D. Sorting and storage during secretory granule biogenesis: looking backward and looking forward. *Biochem J*. 1998;332(pt 3):593–610.
67. Kögel T, Gerdes HH. Maturation of secretory granules. *Results Probl Cell Differ*. 2010;50:1–20.
68. Morvan J, Tooze SA. Discovery and progress in our understanding of the regulated secretory pathway in neuroendocrine cells. *Histochem Cell Biol*. 2008;129(3):243–252.
69. Williams JA. Regulation of pancreatic acinar cell function. *Curr Opin Gastroenterol*. 2006;22(5):498–504.
70. Tian JH, Das S, Sheng ZH. Ca2+-dependent phosphorylation of syntaxin-1A by the death-associated protein (DAP) kinase regulates its interaction with Munc18. *J Biol Chem*. 2003;278(28):26265–26274.
71. Wu PR, et al. DAPK activates MARK1/2 to regulate microtubule assembly, neuronal differentiation, and tau toxicity. *Cell Death Differ*. 2011;18(9):1507–1520.
72. Pelkmans L, et al. Genome-wide analysis of human kinases in clathrin- and caveolae/raft-mediated endocytosis. *Nature*. 2005;436(7047):78–86.
73. Nam KT, Varro A, Coffey RJ, Goldenring JR. Potentiation of oxyntic atrophy-induced gastric metaplasia in amphiregulin-deficient mice. *Gastroenterology*. 2007;132(5):1804–1819.
74. Zhu L, Tran T, Rukstalis JM, Sun P, Damsz B, Konieczny SF. Inhibition of Mist1 homodimer formation induces pancreatic acinar-to-ductal metaplasia. *Mol Cell Biol*. 2004;24(7):2673–2681.
75. Pin CL, Rukstalis JM, Johnson C, Konieczny SF. The bHLH transcription factor Mist1 is required to maintain exocrine pancreas cell organization and acinar cell identity. *J Cell Biol*. 2001;155(4):519–530.
76. Li C, Wong WH. Model-based analysis of oligonucleotide arrays: expression index computation and outlier detection. *Proc Natl Acad Sci U S A*. 2001;98(1):31–36.
77. Zhong S, Li C, Wong WH. ChipInfo: Software for extracting gene annotation and gene ontology information for microarray analysis. *Nucleic Acids Res*. 2003;31(13):3483–3486.
78. Ovcharenko I, Nobrega MA, Loots GG, Stubbs L. ECR Browser: a tool for visualizing and accessing data from comparisons of multiple vertebrate genomes. *Nucleic Acids Res*. 2004;32(Web Server issue):W280–W286.
79. Huh WJ, Mysorekar IU, Mills JC. Inducible activation of Cre recombinase in adult mice causes gastric epithelial atrophy, metaplasia and regenerative changes in the absence of "floxed" alleles. *Am J Physiol Gastrointest Liver Physiol*. 2010;299(2):G368–G380.